

## Monte Carlo approach to tissue-cell populations

D. Drasdo\*

*Max-Planck-Institut für Biophysikalische Chemie, Am Fassberg 11, 37077 Göttingen, Federal Republic of Germany*

R. Kree

*Institut für Theoretische Physik, Bunsenstrasse 9, 37073 Göttingen, Federal Republic of Germany*

J. S. McCaskill

*Institut für Molekulare Biotechnologie, Beutenbergstrasse 11, 07745 Jena, Federal Republic of Germany*

(Received 21 February 1995)

We describe a stochastic dynamics of tissue cells with special emphasis on epithelial cells and fibroblasts and fibrocytes of the connective tissue. Pattern formation and growth characteristics of such cell populations in culture are investigated numerically by Monte Carlo simulations for quasi-two-dimensional systems of cells. A number of quantitative predictions are obtained which may be confronted with experimental results. Furthermore we introduce several biologically motivated variants of our basic model and briefly discuss the simulation of two-dimensional analogs of two complex processes in tissues: the growth of a sarcoma across an epithelial boundary and the wound healing of a skin cut. As compared to other approaches, we find the Monte Carlo approach to tissue growth and structure to be particularly simple and flexible. It allows for a hierarchy of models reaching from global description of birth-death processes to very specific features of intracellular dynamics.

PACS number(s): 87.10.+e

### I. INTRODUCTION

Models of growing biological populations have been extensively studied both in mathematical biology and in theoretical physics. Recent works have considered a widely varying range of topics ranging from problems of evolution at the molecular level (e.g., [1,2]), to epidemiology (e.g., [3,4]) and critical phenomena connected with environmental pollution (e.g., [5]).

Among such topics the problem of *morphogenesis*, i.e., the pattern formation during the growth of cell populations, has found particular interest. Many different approaches have been proposed: these include reaction-diffusion type differential equations (e.g., [6–11]), cellular automata (e.g., [13–18]), and generative grammars (e.g., [19,20]). Some authors try to explain the emergence of forms in biological systems in terms which are reminiscent of condensed matter physics. They explicitly refer to mechanical, or viscoelastic properties of cells ([21–23]) or even treat assemblies of cells like thermodynamic many-body systems ([24–31]).

In the present work we subscribe to this point of view and try to describe the growth, pattern formation, and cell differentiation in epithelial and static connective tis-

sue (fibroblasts and fibrocytes, no cells of the hemopoetic and lymphatic system) by Monte Carlo simulations of assemblies of very simple model cells. The Monte Carlo algorithm provides sample trajectories of a stochastic Markovian cell dynamics (e.g., [32–37]).

Epithelia and connective tissue cells are interesting objects of study because they constitute—beside muscle and nerve cells—two of the four basic types of tissue in higher eucaryotic organisms. Our main emphasis in this work is on epithelia, which constitute the outer and inner boundaries of the organism, separating it from its environment but also enclosing differentiated organs (e.g., in [38]).

As it is not easy to study growing cell populations in a higher organism, cell cultures have become an important tool for the investigation of differentiated eucaryotic cells. Such cultures of cells on special substrates usually form two-dimensional populations (e.g., [39–43]). With the noticeable exception of monolayered epithelial cells, most other tissue structures are three dimensional and therefore one cannot hope to reproduce the biologically correct geometrical arrangement of cells in a cell culture. This is another reason for us to start quantitative investigations of differentiated cells with epithelia. Fully developed, the tissue textures of epithelial cells look quite regular [68] and the shapes of single cells seem to deviate much less from a compact sphere than cells of other types of tissue. This facilitates the modeling as we will see below.

The fibroblasts and fibrocytes of the connective tissue, on the other hand, form a more or less tightly woven network and fill up the intercellular medium with secreted substances like collagen. The cells usually possess a com-

---

\*Present address: Max-Planck-Institut für Kolloid und Grenzflächenforschung, Kantstrasse 55, 14513 Teltow, Federal Republic of Germany. Electronic address: Drasdo@mpikg-teltow.mpg.de

pact soma with offshoots which contribute to the network structure of the tissue [69].

To set up a Markovian dynamics of cells we first have to construct an appropriate state space which must include variables to describe both the geometry and the internal activity states of a cell. Although the geometry of the cell membrane is highly variable and there is a plethora of internal activities within each living cell this does not necessarily exclude a description of *collective* effects in cell assemblies using only a few relevant variables for each cell. Many “microscopic” details of cells may be unimportant for certain aspects of collective behavior.

All our models are based on a highly simplified description of cell shapes. Instead of considering all the geometrical surfaces which may be realized by a cell membrane, we use a coarse-grained description which takes into account the cell shapes only in a statistical sense. We attach to each cell a region in space where most of the cell volume is located with overwhelming probability. The boundaries of these regions define shells around some geometrical surface which marks the *average cell shape* (see Fig. 1). The average shapes may depend on the internal state of a cell (e.g., its age within the proliferation cycle) and thus will generally be time dependent. Obviously this description is limited to cell types with ge-

ometrical shapes which do not deviate too much from an average (cells of the neuronal tissue, e.g., do not belong to this class). For epithelial cells and cells of the connective tissue this assumption seems reasonable. Note that although cell membrane patterns of the tissue cannot be uniquely reconstructed from the statistical description, it remains possible to obtain information on the tissue morphologies within our approach. For example, for densely packed clusters of cells the construction shown in Figs. 1(b) and 1(c) leads to membrane patterns which are almost identical to the real ones if cell contact areas are nearly planar (which is correct for epithelial cells).

Cells interact with each other via surface molecules attached to the cell membrane (e.g., CAM's, i.e., cell adhesion molecules) and via mechanical forces due to the visco-elastic properties of the membrane and the cytoskeleton. Besides these short-range interactions there are also long-range interactions due to substances which are secreted by one cell, diffuse or flow through the extra cellular medium, and are felt (via receptor molecules) by other cells which respond by a change of internal activities. In the following we only consider the short-range interactions which play an important role for the stability of tissue structures as has been demonstrated in a number of experiments (e.g., [44–48]).

The life history of a proliferating cell begins after its creation by cell division. Here we roughly distinguish between two age classes, the *interphase* and *mitosis*. During the interphase the cell is steadily growing until it has doubled its mass, its organelles, and its DNA content. Then it enters mitosis where it deforms until the next cell division is completed. During its entire life history a cell may migrate and (if it is not spherically symmetric) rotate. Cooperative effects arise, because all its activities are influenced by interactions with other cells. For example, a growth trial will not always be successful due to the contact inhibition by neighboring cells and a migration trial may fail if the cell is tightly bound to a cell cluster.

To take such effects into account we model the cell interaction by potentials  $V$  and accept the trial of an activity only with probability  $\propto \exp(-\Delta V)$  whenever the trial will increase the interaction potential, i.e., when  $\Delta V > 0$ . This corresponds to the standard prescription of the Metropolis algorithm [49], which is used frequently to obtain statistical samples of equilibrium distributions. Note, however, that due to the intrinsic birth process a cell population in an unbounded system will grow indefinitely (unless cells stop to proliferate) and will never reach an equilibrium or stationary state. In the present work we use the Monte Carlo method to simulate the stochastic dynamics, which is defined by the transition probabilities. The use of the Monte Carlo approach to study kinetic phenomena depends critically on the choice of elementary steps: in particular, whether the transition states are included as intermediates in the state space or not. In this case, attention has been given to find the appropriate states as seen below (e.g., [35–37]).

Experimentally, tissue cells are studied *in vivo* as well as in cell cultures. The latter have become an important experimental tool for the investigation of tissue cells (e.g.,

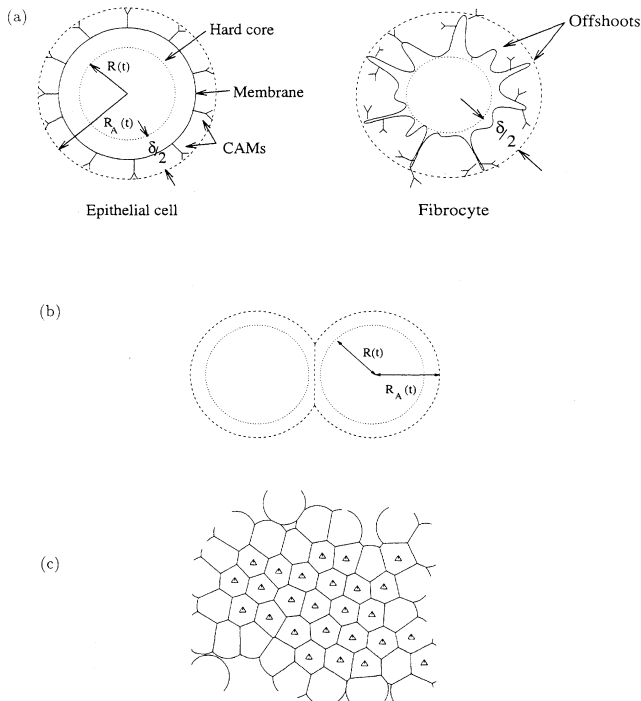


FIG. 1. (a) Statistical description of cell shapes. Cell membrane configurations are confined to the indicated shell of width  $\delta/2$ . (b) Reconstruction of membrane configuration at cell contacts. Contact lines are assumed to be straight. (c) Example of a tissue structure reconstructed from the statistical description.

[39–43]). These cultures can be regarded as quasi-two-dimensional structures. As they are more accessible to quantitative experimental methods and at the same time can be simulated with considerably less effort than three-dimensional structures, we restrict most of our present work to such systems. We like to stress, however, that this restriction is not essential. All our algorithms can be used for three-dimensional systems with only minor modifications.

In the next section, we will give a detailed description of our modeling strategy and describe the basic model for proliferating tissue cells. Several biologically motivated variants will be introduced in a separate subsection. They allow us to simulate more realistic and more complex histological processes. At the end of this section we introduce the quantities which we used to characterize the growth and structure of cell assemblies. Section III contains the presentation and discussion of our results for monoclonal cell assemblies. In Sec. IV we outline how to simulate more complex histological processes. As we consider two-dimensional systems, we can only study analogs of situations appearing in three-dimensional tissue *in vivo*. However, even these strongly simplified analogs display interesting features and help one to understand how theoretical modeling may interact with experimental investigations. In the final section we give a discussion of the proposed method and the results obtained, speculate on possible applications, and mention some open questions for future work. A detailed presentation of the simulation algorithm is given in the Appendix.

## II. A MODEL OF TISSUE CELLS

### A. Statistical description of cell shapes

A lipid double membrane separates the cell from its environment. It also provides a selective diffusion barrier and takes part in cell-cell recognition, signal processing, and cell/cell connections (e.g., [50]). The cell membrane contains glycoproteins and glycolipids, which are responsible for short-range interactions between cells.

A difficulty which one immediately meets in any attempt to model an assembly of growing and interacting cells consists in finding an adequate description for the highly variable shapes of the cell membrane. Even the average shape of a cell does not only depend on the cell type (epithelial, connective tissue, etc.), but also on its age within a proliferation cycle and on contacts with other cells. In the following we introduce a statistical, coarse-grained model of cell shapes which does not attempt to describe all the possible fluctuations of the cell membrane in detail. We propose this model as a simple but still adequate description of epithelial cells and possibly also of fibroblasts and fibrocytes.

As our main emphasis is on cells in culture, we will sometimes refer to two-dimensional geometrical constructs explicitly. (The reader may immediately generalize the model to three-dimensional tissue.) In our simulations we assume a cylindrical symmetry of average cell shapes. Thus the average shapes can be reconstructed

uniquely from (one-dimensional) boundary lines in the plane of the substrate. Note that epithelial cells possess convex, polygonal shapes both *in vivo* and in culture [Fig. 1(c)].

Even the average shape of a single cell is not constant. Most noticeably, a cell grows and strongly deforms during its proliferation cycle. Within one proliferation cycle we distinguish between two age classes (see Fig. 2): the interphase (*I* cells) and the mitotic phase (*M* cells). We will take into account that the average shapes of *I* and *M* cells are very different. Therefore we will discuss them in sequence.

#### 1. Interphase cells (age class *I*)

During the interphase, an *I* cell grows to double its mass, its organelles, and its DNA content. To describe its possible shapes, we attach a circle (in a 2D cell culture) of radius  $R(\tau)$  to each *I* cell of age  $\tau$  within the proliferation cycle. At the beginning of the interphase  $R(\tau = 0) = R_{\min}$ . We assume that shape fluctuations

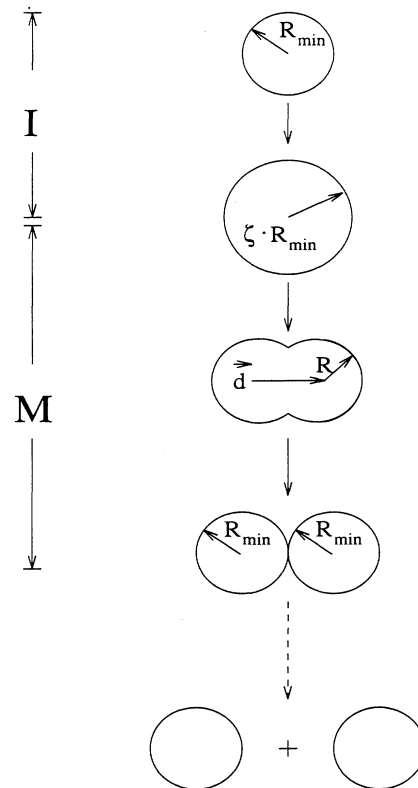


FIG. 2. Development of average cell shape during a proliferation cycle. At the beginning of the *I* phase, the cell radius is  $R_{\min}$ .  $R$  will grow until the cell mass is doubled. In the *M* phase the distance  $d$  between the two centers of the symmetrical dumbbell shape is growing until  $d = 2 \times R_{\min}$ . At the same time the radius  $R$  shrinks to keep the cell volume constant.

are restricted by the requirement that the distance between the cell membrane and the center of the cell body never becomes smaller than  $R(\tau)$ . This constraint can be implemented as a hard core potential of radius  $R(\tau)$  which is seen by the membrane. Physically, shape fluctuations are limited by cell compressibility and viscoelastic deformation energies of the cell membrane and the cytoskeleton. If the cell shapes do not fluctuate too much (both in time and within the cell assembly), i.e., most of a cell's mass and volume are concentrated in a compact soma, the assumption of an incompressible spherical part seems a reasonable approximation (e.g., cells of neuronal tissue, do not fall into this class). Within a shell  $(R(\tau), R(\tau) + \delta/2)$  of width  $\delta/2$  the fluctuating cell membrane may interact with other cells. Thus  $\delta$  sets the length scale of short-range cell-cell interactions which are mediated, for example, by cell adhesion molecules (CAM's). On the other hand,  $\delta$  also determines the average geometrical cell shape which is the three-dimensional reconstruction from a circle of radius  $R + \delta/4$  in the plane, of the substrate. (As we will only use the cell properties within this plane we will also refer to the circle as the average cell shape.) Thus cell interaction and cell shape are not independent in a coarse-grained description.

It is an advantage of this description that one can consider even these cells as convex which assume convex shapes only in a statistical sense. Therefore we propose to apply this type of modeling also to fibroblasts and fibrocytes of the connective tissue. The membrane offshoots of these cells will lead to a coarse-grained interaction which is of much longer range than the underlying chemical bonds of CAM's whereas the average cell shape—and noticeably the incompressible part of the cell body—remains spherical (see Fig. 1). For such cells an interaction potential which decreases continuously with distance (instead of the potential described above with finite cutoff  $\delta/2$ ) may be more appropriate. The range of the interaction is not so easy to estimate but is certainly larger than one average cell diameter for many connective tissue cells.

A lower bound for  $\delta$  can be estimated from the length of a sugar residue of a typical surface glycoprotein in the nm range while cells are in the  $\mu\text{m}$  range (which leads to  $\delta \approx 0.2R_{\min}$  [51]). For epithelial cells we expect interaction ranges that are not much different from this value.

Having noticed that membrane fluctuations lead to a coarse-grained cell interaction we proceed and model this interaction by a phenomenological (attractive) "potential"  $V(r)$  which is seen by the membranes of other cells. Its form and its influence on the cell dynamics will be discussed in the next subsection.

In general the statistical description does not allow one to reconstruct the membrane configurations uniquely. For densely packed cell clusters, however, the simple geometrical construction shown in Figs. 1(b) and 1(c) will lead to a one-to-one correspondence between a configuration of spheres (circles) and cell membrane polygons of the actual cell shapes, provided the contact areas (lines) between cells are planar (straight). This is justified for epithelial cells. For the cells of the connective tissue, on

the other hand, the construction may not lead to sensible results because of the long range of interactions. In this case we can obtain geometrical information by performing a Voronoi construction to extract the regions of space which are dominated by specific cells. Our model may also be generalized to cell types with nonspherical average shapes by replacing the spherical hard core by an ellipsoid.

An  $I$  cell will grow until it has doubled its volume and mass. Thus after the circle of the average cell shape exceeds a radius  $R_{\max} = \zeta R_{\min}$ ,  $\zeta > 1$  corresponding to doubled volume, it enters the age class  $M$ . The precise value of  $\zeta$  depends on the three-dimensional cell shape. In most of our simulations we used  $\zeta = \sqrt{2}$ , which corresponds to cylindrical prisms.

## 2. Mitotic cells (age class $M$ )

Biologically, the interphase stops with the beginning of the so-called *prophase*, during which the cell reduces its surface structure and its protein synthesis ([52–55]). Our age class  $M$ , however, mainly refers to the last phase of mitosis, i.e., the *telophase* during which the cell develops through symmetrical dumbbell shapes into two spherical cells of the next generation. We checked that the results presented here do not depend critically on the exact shape of the cells during mitosis. This deformation appears at approximately constant volume. Figure 3 shows the evolution of coarse-grained cell shapes during a proliferation cycle. A dumbbell is described by the vector  $\vec{d}$  joining its centers  $\vec{r}^{(1)}$  and  $\vec{r}^{(2)}$ . Due to the volume constraint,  $\vec{d}$  also determines the radius of the two spheres (circles)  $R^{(1)} = R^{(2)} = R$ . It should be mentioned that an approach with a planar dumbbell or an approach where the deformation process is accompanied directly by the area increase also works, while a purely spherical approach without deformation of the cell (where the division step is strongly discontinuous) does not lead to useful results [56].

An  $M$  cell will increase the distance  $d$  between the two centers of its dumbbell until the two cells of the next generation appear as separated spheres with radii  $R_{\min}$ . While  $d$  is growing, the radii of the two spheres (circles) forming the dumbbell have to shrink such that the cell volume is kept approximately constant.

## B. Stochastic cell dynamics

The state  $S_i$  of a cell  $i$  is described by its position, its age class, and its shape. The cell position is given by the vector  $\vec{r}_i$  of its center of mass. For an  $I$  cell, the shape is characterized by its radius  $R_i$ , whereas for an  $M$  cell it is the vector  $\vec{d}_i$  joining the centers of the corresponding dumbbell which fixes its shape. As the radii  $R_i^{(1)} = R_i^{(2)} = R_i$  of the spheres making up the dumbbell are equal and furthermore determined by the length of  $\vec{d}_i$ , we may also describe the shape by  $R_i$  and a

unit vector  $\hat{d}_i$  which fixes the orientation of an  $M$  cell in space.

During a single updating step, only one randomly chosen cell is considered as active and tries to perform one of the following actions  $\alpha$ : (i)  $\alpha^I \in \{\text{migration, growth}\}$  for  $I$  cells, (ii)  $\alpha^M \in \{\text{migration, rotation, deformation}\}$  for  $M$  cells.

A single migration trial consists of a shift  $\vec{r}_i \rightarrow \vec{r}_i + \delta\vec{r}_i$  of cell  $i$  in a random direction with a step length which is chosen at random out of an interval  $[0, \delta r_{\max}]$ . A rotation trial is defined analogously. During a growth step, the radius of an  $I$  cell is increased by a random amount  $\delta R \in [0, \delta R_{\max}]$  whereas during a deformation step the length of  $\vec{d}$  is increased and at the same time the dumbbell radius is decreased such that the volume of the cell is kept constant. All these trials are described in detail in the Appendix.

Whether cell  $i$  actually performs its chosen trial or not depends on its interaction with other cells. Following the discussion of the preceding subsection, we model the interaction between two cells  $i$  and  $j$  by potentials  $V_\alpha(S_i, S_j)$ . Note that these interaction potentials may be different for different types of actions  $\alpha$ . We will discuss the biological basis of this complication below.

The cell dynamics is based on the assumption that a trial is accepted according to the standard prescription of the Metropolis algorithm [49], i.e., an action  $\alpha$  is always accepted if the change of the state  $S_i \rightarrow \bar{S}_i$  of cell  $i$  induced by  $\alpha$  leads to a decrease of its interaction potential with other cells  $E_\alpha(S_i) = \sum_j V_\alpha(S_i, S_j)$ , whereas it is only accepted with probability  $\exp(-[E_\alpha(\bar{S}_i) - E_\alpha(S_i)])$  if  $E_\alpha(S_i)$  is increased by  $\alpha$ .

In order to describe the cell behavior in accordance with biological facts we have to allow for age class and activity-dependent interaction potentials. In our basic model (which will be called model  $A$  henceforth) we assume that the migration of  $I$  cells is controlled by a spherically symmetric two-body ‘‘potential’’  $V^{II}(i, j) = V^{II}(|\vec{r}_i - \vec{r}_j|)$ .  $V^{II} = V_{\text{HC}}^{II} + V_{\text{attr}}^{II}$  is composed of a hard-core part  $V_{\text{HC}}^{II}$  corresponding to the incompressible cell core and an attractive part  $V_{\text{attr}}^{II}$  due to chemical or mechanical bonds between the membranes of the interacting cells. The functional form of  $V_{\text{attr}}^{II}(r)$  depends on the details of the interaction mechanisms. For most of the simulations of the present work, we used a square-well form, i.e.,  $V_{\text{attr}}^{II} = -\epsilon = \text{const}$  within the interaction range [see Fig. 3(a)]. With  $R_{ij}(\tau) := R_i(\tau) + R_j(\tau)$  we thus get

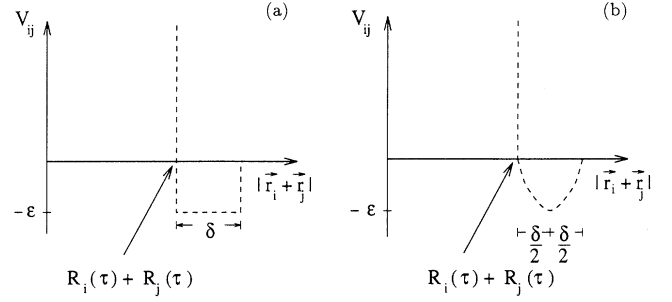


FIG. 3. The two forms of interaction potentials between cells: (a) square-well potential and (b) harmonic well.

$$V^{II}(i, j; \tau) = \begin{cases} \infty & \text{for } |\vec{r}_i - \vec{r}_j| \leq R_{ij}(\tau) \\ -\epsilon & \text{for } R_{ij}(\tau) \leq |\vec{r}_i - \vec{r}_j| \leq R_{ij}(\tau) + \delta \\ 0 & \text{otherwise.} \end{cases} \quad (1)$$

Note that this potential will change in time due to the change of the average cell shapes. We also considered a harmonic well potential (restricted to the interaction shell) [see Fig. 3(b)]. This form of a potential contains an increasing energy gain from larger contact areas which one would expect for chemical bonding between CAM’s distributed on the cell membrane with a constant density. In Sec. IV we will illustrate biological effects which result from changes in the functional form of the interaction potential.

In contrast to cell migration, the dynamics of growth and deformation steps of model  $A$  depends only on the hard-core part  $V_{\text{HC}}$ . This corresponds to the assumption that cell growth (as well as cell division) steps are not influenced by the existence of chemical bonds between surface molecules but still have to respect the limited cell compressibility. Several biologically motivated variants of the dependence of interactions on activities and age classes will be introduced in the next subsection.

During all cell interactions an  $M$  cell is treated like a composite of two, partially overlapping spherical cells. The total interaction energy of two  $M$  cells is assumed to be independent of the size of the cells. Thus, e.g., the total interaction energy between two  $M$  cells, for example, is of the form

$$V_\alpha^{MM}(i, j; \tau) = \begin{cases} \infty & \text{for } |\vec{r}_i^{(k)} - \vec{r}_j^{(l)}| \leq R_{ij}(\tau) \\ & \text{with } k, l = 1, 2 \\ f_\alpha(i, k; j, l; \tau) & \text{for } R_{ij}(\tau) < |\vec{r}_i^{(k)} - \vec{r}_j^{(l)}| < R_{ij}(\tau) + \delta \\ & \text{for at least one } k \in \{1, 2\} \text{ and one } l \in \{1, 2\} \\ 0 & \text{for } R_{ij}(\tau) > |\vec{r}_i^{(k)} - \vec{r}_j^{(l)}| + \delta \\ & \forall i, j \text{ with } i \neq j \text{ and } k, l = 1, 2. \end{cases} \quad (2)$$

Here,  $i, j$  are the cell indices,  $k$  is the index for the two overlapping circles forming cell  $i$ ,  $l$  is the index for the two overlapping circles forming cell  $j$ , and  $f_\alpha(i, k; j, l; \tau)$  is defined by

$$\begin{aligned}
f_\alpha(i, k; j, l; \tau) = & [V_\alpha(|\vec{r}_i^{(1)} - \vec{r}_j^{(1)}|; \tau) + V_\alpha(|\vec{r}_i^{(1)} - \vec{r}_j^{(2)}|; \tau) + V_\alpha(|\vec{r}_i^{(2)} - \vec{r}_j^{(1)}|; \tau) \\
& + V_\alpha(|\vec{r}_i^{(2)} - \vec{r}_j^{(2)}|; \tau)] / [\Theta(R_{ij}(\tau) + \delta - |\vec{r}_i^{(1)} - \vec{r}_j^{(1)}|) + \Theta(R_{ij}(\tau) + \delta - |\vec{r}_i^{(1)} - \vec{r}_j^{(2)}|) \\
& + \Theta(R_{ij}(\tau) + \delta - |\vec{r}_i^{(2)} - \vec{r}_j^{(1)}|) + \Theta(R_{ij}(\tau) + \delta - |\vec{r}_i^{(2)} - \vec{r}_j^{(2)}|)].
\end{aligned}$$

Here the upper indices on the right-hand side refer to the two circles which determine the average shape of the  $M$  cell. In general interaction  $V_\alpha$  will consist of a hard-core part and possibly of an attractive part which need not, however, be equal to the interaction between two  $I$  cells.

A polarity of cells which results in an anisotropic expression of CAM's can be taken into account by an appropriately modeled angular dependence of the attractive part of the interaction potential (see Fig. 4). In some simulations we considered cells which possess a polar direction  $\hat{n}$  such that there exists a sector of angular width  $\Delta\phi$  around  $\hat{n}$  where attractive surface molecules are located whereas the interaction between two such polar cells is strongly repulsive outside this sector. This interaction stabilizes one-dimensional topologies of rings and chains [see Fig. 4(b)] (surfaces of spherical or plane topology in the three-dimensional analog are stabilized if attractive and repulsive regions are interchanged so that a cell potential is repulsive in the angular vicinity of its poles and attractive within a circular ring around the equator). For these polar cells we use model potentials of the form

$$\begin{aligned}
U(\vec{r}_i, \vec{r}_j, \hat{n}_i, \hat{n}_j) = & V_{\text{HC}}(|\vec{r}_i - \vec{r}_j|; \tau) + V_{\text{attr}}(|\vec{r}_{ij}|; \tau) \\
& \times f(\hat{r}_{ij} \cdot \hat{n}_i) f(\hat{r}_{ij} \cdot \hat{n}_j).
\end{aligned} \quad (3)$$

Here  $\vec{r}_{ij} := \vec{r}_i - \vec{r}_j = |\vec{r}_{ij}| \hat{r}_{ij}$ ,  $V_{\text{HC}}$  is the spherical hard core, and  $V_{\text{attr}}$  is one of the spherically symmetric attractive potentials introduced above, so that  $V_{\text{attr}} \leq 0$ . The function  $f$  selects the attractive and repulsive sectors. In our two-dimensional simulations we used

$$f(\cos \phi) := \begin{cases} f_0 \gg 1 & \text{for } |\phi| \leq \Delta\phi \\ 0 & \text{for } |\phi| > \Delta\phi. \end{cases} \quad (4)$$

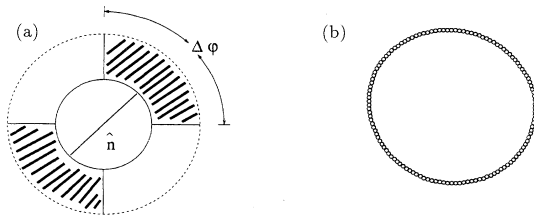


FIG. 4. Interaction between polar cells. (a) Within the hatched sector the interaction is attractive. (b) Once a closed ring is formed the anisotropic potential stabilizes the ring topology even for a growing population.

Although the above prescriptions are very simple models of the complicated active cell processes which take place during migration, growth, and cell division, they nevertheless account for salient biological facts. They take into account contact inhibition and cell adhesion as factors which modify cell migration and at the same time contain a density regulation mechanism of growth and proliferation. Furthermore, they provide flexible frameworks for the inclusion of more specific biological mechanisms, as will be discussed subsequently.

To complete the introduction of our model of cell dynamics we will now discuss the time scales  $\tau$  for the different age classes and different cell activities  $\alpha$ . In some of our simulations we varied the ratio  $f^{IM} = T^I/T^M$  of the average lengths of the time intervals that a single, noninteracting cell spent in the  $I$  phase and in the  $M$  phase ( $T^I$  and  $T^M$ , respectively). We find that  $f^{IM}$  is increased by a factor of  $\approx 3$  due to interaction effects. If we use typical experimental values from tissue (see e.g., [57]) of 26 h for the cell cycle time and 1–2 h for  $T^M$ , i.e.,  $f^{IM} \approx 12$ –25 we conclude that the ratio should be chosen  $f^{IM} \approx 4$ –8 to correctly reproduce the observed value in tissue. For most of our results which we will discuss below, however, we used  $f^{IM} = 1$  for simplicity (we carried out computer simulations with selected values for the growth rate and the diffusion rate, and it turns out that  $f^{IM} \approx 8$ –20 for interacting cells depending on the growth rate due to the interaction of cells in the cell population if  $f^{IM} = 4$  for a single free cell [56]).

We always assumed that  $\tau_{\text{rot}} \leq \tau_{\text{mig}} \ll \tau_{\text{growth}} \approx \tau_{\text{def}}$  which is reasonable for the cell types we considered. The relative time scales are fixed by fixing the number of rotation updates  $\nu_{\text{rot}}$  per migration update and the number of migration updates  $\nu_{\text{mig}}$  per growth-deformation update. Typical values are  $\nu_{\text{rot}} = 1$ –10 and  $\nu_{\text{mig}} = (5 \times 10^0)$ – $(5 \times 10^3)$ . The quantity

$$r_g := \frac{1}{\tau_{\text{mig}}} \quad (5)$$

is a measure of the intrinsic growth rate of the cells and will be used as a basic model parameter in the following.

The total number of update steps is related to *real time* by enhancing  $t \rightarrow t + \Delta t$  in an assembly of  $N(t)$  cells after  $N(t)$  migration updates. In this way  $\Delta t$  corresponds to the time scale for migration of an isolated cell which can be estimated from measuring its diffusion constant  $D$  and using  $D \simeq (\overline{\delta\vec{r}})^2 / (4\Delta t)$ , where  $(\overline{\delta\vec{r}})^2 = 0.5(\delta r_{\text{max}})^2$  is the variance of the distribution of migration steps used in the simulation. A flow chart diagram of the basic simulation algorithm is depicted in the Appendix [see Fig. 34].

### C. Variants of the basic model

We have studied several variants of the above described model *A* which are motivated by biological observations [58,59]. In fact, the growth behavior of model *A* cells is more like that of malignant tumor cells than like normal tissue. For example, model *A* cells never leave the proliferation metabolism to become differentiated tissue cells. By introducing variants which take into account more and more properties of normal tissue cells it becomes possible to investigate how certain changes in cell behavior (e.g., transformation into malignant tumor cells) are reflected by the growth patterns of cell cultures.

*Model A.* In our basic model, the mobility of *I* and *M* cells is identical and the interaction potential depends only on the cell activity, but not on the age class, i.e.,

$$V = \begin{cases} V_{\text{HC}} + V_{\text{attr}} & \text{for migration and rotation} \\ V_{\text{HC}} & \text{for growth and deformation.} \end{cases} \quad (6)$$

*Model B.* Cells reduce their number of surface molecules during mitosis, which leads to a reduction of the attractive cell adhesion in age class *M*. To study the effects of this reduction we switched off  $V_{\text{attr}}$  during age class *M*:

$$V = \begin{cases} V_{\text{HC}} + V_{\text{attr}} & \text{for migration of } I \text{ cells} \\ V_{\text{HC}} & \text{otherwise.} \end{cases} \quad (7)$$

*Model C.* The mobility of *M* cells can be much higher than that of *I* cells. In fact, many cells in the interphase have a tendency to build up mechanical contacts with the substrate which are reduced during mitosis (e.g., [52–55]). Therefore we considered a model which is characterized by the interaction potential of model *B* and age class dependent  $\nu_{\text{mig}}$ ,

$$\nu_{\text{mig}} = \begin{cases} \nu_{\text{mig}}^I & \text{for } I \text{ cells} \\ \nu_{\text{mig}}^M = 10\nu_{\text{mig}}^I & \text{for } M \text{ cells.} \end{cases} \quad (8)$$

*Model D.* This variant of model *A* takes into account the possibility of cell death. After each cell division one of the daughter cells is killed with probability  $p_D$ . Thus we describe a birth-death process which reaches its critical point at  $p_D = 1$ . (In the present work we are not interested in the universal properties near this critical point.) Such a situation may correspond to a low-dose treatment of a growing tumor with drugs or radiation.

*Model E.* This model introduces mechanisms which may lead to stable tissue patterns by a collective regulation of cell differentiation. We assume that a cell leaves the proliferation cycle to become a functioning tissue cell according to criteria which are based on the local neighborhood of this cell. In Sec. IV we will present results based on one of the following two criteria: cell *i* switches from proliferation to tissue function if (i) the number of interaction partners  $n_i$  reaches a threshold value  $n_c$  and (ii) the change in cell radius after a fixed number (20) of trials remains below a threshold  $|R_i(t+20) - R_i(t)| \leq R_c$  due to blocking by other cells. Other criteria which depend on cell polarity will be discussed elsewhere [56,60].

*Model F.* In some simulations (see Sec. IV) we needed polar cells with an anisotropic interaction potential of

the form Eqs. (3) and (4), which influence migration, growth, and the axis  $\vec{d}$  of cell division. For a more detailed discussion of polar cells we refer the reader to Refs. [56,60].

### D. Simulations

In our first type of simulations we started from one cell individual at the beginning of age class *I* and usually stopped when the cell assembly consisted of 800 cells. We also performed some runs with up to 5000 cells to check whether the results obtained from the growth of the 800 cell assemblies remained stable.

In Sec. IV we describe simulations with two different types of cells. In these simulations we started from a macroscopic pattern of epithelial cells (a monolayered circular ring) which we created with model *F* cells (see Fig. 4 and Fig. 29). In addition, the initial configuration consisted either of a single model *A* cell in the center of the ring or of 800 model *E* cells which fill up the circle. We consider the first scenario as a rough approximation of a growing sarcoma reaching an epithelial boundary as will be discussed in Sec. IV. In the second scenario, the initial configuration was disturbed by cutting out a sector of cells. Afterwards, we observed the healing process to study whether and how the original macroscopic pattern was reconstructed. Although this still remains a crude model for a wound healing process (see [56,60]), we believe that it already contains crucial regulation mechanisms which can be tested against experiments.

The maximal step width for migration, rotation, growth, and deformation were adjusted such that those evolution histories which should be impossible in real cell assemblies were never observed. This led us to  $|\delta\vec{r}_{\text{max}}| = R_{\text{min}}/6$  for migration,  $\delta\alpha_{\text{max}} = \pi/4$  for rotations. During a growth step as well as during a deformation step the radius of a circle was changed by at most  $\delta R_{\text{max}} = R_{\text{min}}/12$ . To avoid boundary effects due to drift of the center of mass of the whole cell assembly we used periodic boundary conditions with a quadratic unit cell of length  $L = 1$ . For a population of up to 800 cells we chose  $R_{\text{min}} = 0.007$ , for larger populations we scaled down the cell radius accordingly, so that always  $L \approx 140R_{\text{min}}$ . If not stated otherwise in the text we use an interaction range  $\delta = 0.2R_{\text{min}}$  as discussed above.

### E. Characterization of cell assemblies

From our simulation data, we evaluated a number of quantities which are useful to characterize the growth and structure of cell assemblies.

(a) *Total number of cells*  $N(t)$ . The number of cells  $N(t)$  as a function of real time.

(b) *Morphology*. For increasing sizes  $n = k \times 100$  with  $k = 1, 2, 3, \dots, 8$  of a population, we plotted the cell shapes, i.e., the boundaries of the incompressible parts of the cells of the assembly. These plots display the complete geometrical information contained in the state of the cell assembly.

(c) *Cluster size distribution*  $n(s)$ . The number and size

of connected subpopulations (*clusters*) of the final cell assembly are shown in diagrams which depict number  $n$  of clusters versus cluster size  $s$ . Two cells are considered as connected if their distance is less or equal to the maximal interacting distance, i.e., they belong to one *cluster*.

(d) *Cluster masses and boundary lengths*  $M(C)$ ,  $\ell(\partial C)$ . The boundary  $\partial C$  of a cluster  $C$  is defined as the shortest polygon which joins all the centers of boundary cells. The cluster mass is taken to be proportional to the total area covered by the cells of the corresponding cluster. We studied the scaling of the length  $\ell(\partial C)$  of the boundary with cluster mass  $M(C)$ .

(e) *Density profile*  $\rho(|\vec{r} - \vec{R}_{c.m.}|)$ . The number of cells per area as a function of the distance from the center of mass of the assembly. This quantity was calculated by ordering the final cells into groups of 50 cells in circular rings according to increasing distance from  $\vec{R}_{c.m.}$ .

(f) *Space filling profile*  $\rho^A(|\vec{r} - \vec{R}_{c.m.}|)$ . Instead of the number of cells,  $\rho^A$  gives the fraction of area covered by cells.

(g) *Statistics of interaction partners*. We evaluated the frequency  $p(n)$  of cells with  $n$  interaction partners and the spatial profile of the average number of partners  $\bar{n}(|\vec{r} - \vec{R}_{c.m.}|)$ . From  $p(n)$ , the mean number of interaction partners of a cell in the final population  $\bar{n}$  and its standard deviation was evaluated.

(h) *Age distribution*  $N(\tau; t_f)$ . We define an age of a cell  $i$  in a cell assembly which developed out of one cell individual at  $t = 0$  up to time  $t_f$  as the difference between  $t_f$  and the time of "birth" of cell  $i$ .

(i) *Subclone statistics*. The number and distribution of offspring of all the cells has been evaluated. We present diagrams which show the number of offspring of each cell in chronological order by counting all the cells according to their appearance (again, one of two daughter cells in every cell division inherits the ordering number of the mother cell). We also present figures which show the morphologies of subclones.

(j) *Generation statistics*. The initial cell constitutes the generation number 0. After each division of a cell of generation  $g$ , both daughter cells belong to generation  $g + 1$ . We calculated the frequency  $p(g)$  of cells of generation numbers  $g$  and the average generation number profile  $\bar{g}(|\vec{r} - \vec{R}_{c.m.}|)$ .

(k) *Statistics of cluster forms*. To get an impression of the temporal development of cluster forms we introduced polar coordinates centered at  $\vec{R}_{c.m.}$  of a cluster and plotted the distance  $d(\phi, t) = |\vec{r}_{\text{boundary}}(\phi, t) - \vec{R}_{c.m.}(t)|$  as a function of the polar angle  $\phi$  for various times  $t$ . From angular averaging of  $d(\phi)$  we obtained the average cluster radius  $\bar{R}_C(t) = \langle d(\phi, t) \rangle$ . Its variance  $\Delta R_C(t) = \sqrt{\langle (\Delta d(\phi, t))^2 \rangle}$  is a measure of boundary roughness. As an alternative measure we also considered a boundary width defined as  $\max\{d(\phi) - d(\psi)\}$  for  $0 \leq \phi, \psi < 2\pi$ . Finally we evaluated the temporal correlation of local roughness, i.e.,

$$C(t, \bar{t}) = \frac{\langle \Delta d(\phi, t) \Delta d(\phi, \bar{t}) \rangle}{\Delta R_C(t) \Delta R_C(\bar{t})}. \quad (9)$$

To perform the angular averaging numerically, we grouped cells into angular intervals of width  $\pi/12 - \pi/9$ .

### III. PROPERTIES OF MONOCLONAL CELL POPULATIONS

#### A. Noninteracting populations

To facilitate the understanding of the simulation results presented below, we first briefly reconsider the growth of an interaction free cell assembly. In this case the proliferation cycle and migration behavior of each cell is completely independent from the other cells.

The life history of a cell consists simply of a sequence of migration steps corresponding to a random walk and of growth or deformation steps. With the above choice of parameters and  $f^{IM} = 1$ , an  $I$  cell needs  $\approx 10$  successful growth trials to reach the  $M$  phase where it also takes  $\approx 10$  deformation trials for the completion of cell division. Thus on the average, the doubling of a cell population takes 20 growth and deformation steps corresponding to  $\tau_2 \approx 20/r_g$  time steps. The noninteracting population will grow exponentially with a characteristic time scale  $\tau_0 = \tau_2 / \ln 2 \approx 1.4\tau_2$ . Due to the diffusive motion, cells separate from each other and the length scale of the assembly grows like  $\sqrt{t}$ . On the other hand, the assembly is growing exponentially due to cell proliferation and thus we can calculate a crossover time  $t_{cr}$  (beyond which cell interaction effects must become important) from the requirement that the length scale of growth becomes larger than the diffusive length scale. This leads to

$$l_{\text{diff}}(t_{cr}) = l_{\text{growth}}(t_{cr})$$

i.e., (10)

$$\text{const} \times \sqrt{t_{cr}} \approx \exp(t_{cr}/2\tau_0) - 1$$

with  $\text{const} \approx \sqrt{\langle \bar{r}^2 \rangle} / \bar{r} \approx 0.1$ .  $\text{const}$  can be calculated from the typical diffusion length in two dimensions using the central limit theorem and comparing the result with the solution of the homogenous problem represented by a two-dimensional diffusion equation. This leads to a diffusion constant of  $D \approx (\delta \bar{r}^2) / (4\Delta t)$ , where  $\langle \bar{r} \rangle = \bar{0}$  and  $\langle \bar{r}^2 \rangle = \delta r_{\text{max}}^2 / 2$  (see the Appendix and Sec. II C).  $\bar{r}$  is the mean radius of a cell, and can be calculated by

$$\bar{r} = \frac{1}{2\pi N} \int_0^N \int_0^{2\pi} v(\phi, m) d\phi dm,$$

where  $v(\phi, m)$  denotes the distance from the construction point  $(x, y)$  of the cell to the border of the cell and depends on the angle for  $M$  cells.

Table I contains a list of crossover times for the growth rates used during our simulations. Furthermore this table displays the total time necessary to build up a population of 800 individuals  $t_0(800)$  and the total length of the diffusive path of a single cell  $l_0(800)$  during this time.

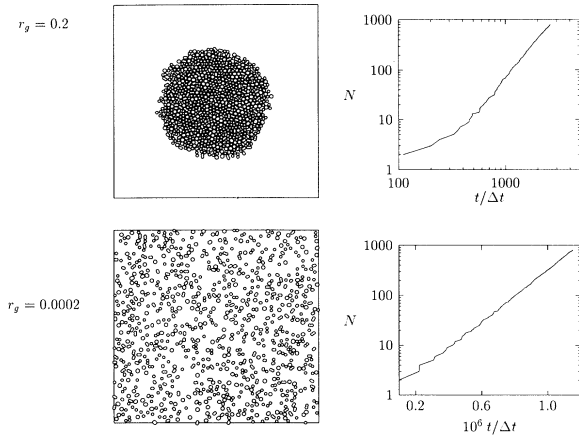


FIG. 5. Morphologies and growth law  $N(t)$  without attractive interaction ( $\epsilon = 0$ ).

Note that for our smallest growth rates, the crossover time exceeds  $t_0(800)$  and  $l_0(800)$  is of the order of the system size  $L \approx 140$ . Therefore we expect to observe exponential growth over the entire simulated time interval. In the absence of attractive interactions the corresponding assemblies should be homogeneously distributed over the entire simulation area. To estimate absolute time and length scales assume an average cell cycle time of  $26h \approx 9.4 \times 10^4$  sec, a mitosis time  $T^M \approx 1-2$  h, and a cell diameter of  $\approx 5-25 \mu\text{m}$ . Then a single updating time step  $\approx 9.4 \times 10^4 / (20\nu_{\text{mig}})$  shrinks from 940 sec for high growth rates ( $r_g = 0.2$ ) to 0.94 sec for our lowest

TABLE I. Useful time and length scales obtained from noninteracting cells.  $r_g$  denotes the growth rate,  $\tau_0$  the doubling time of the population,  $t(800)$  the number of time steps necessary (move updates per cell) to produce a population of 800 cells, and  $l_0(800)$  the diffusion length for a single cell during the time  $t(800)$ .  $t_{\text{cr}}$  is the crossover time defined in Eq. (10).

$r_g$	$\tau_0$	$t_{\text{cr}}$	$t_0(800)$	$l_0(800)$
0.2	140	90	$1 \times 10^3$	3.16
0.1	280	504	$2 \times 10^3$	4.47
0.01	$2.8 \times 10^3$	13720	$2 \times 10^4$	14.14
0.001	$2.8 \times 10^4$	$2.16 \times 10^5$	$2 \times 10^5$	44.72
0.0002	$1.4 \times 10^5$	$1.33 \times 10^6$	$1 \times 10^6$	100

growth rate  $r_g = 0.0002$ . A cell will migrate between  $\approx 1.5 \mu\text{m}$  and  $\approx 250 \mu\text{m}$  within one cell cycle depending on its intrinsic growth rate.

## B. Growth and geometry

In the next two subsections we discuss our results for monoclonal growth of cell populations which are generated by model A. Figures 5, 6, and 7 show morphologies of final cell populations and the number of cells versus time for low ( $r_g = 0.0002$ ) and high ( $r_g = 0.2$ ) intrinsic growth rates and for various strengths of the attractive cell interaction, including the case  $\epsilon = 0$ . Figure 8 shows the population growth for an intermediate growth rate  $r_g = 0.01$ . By comparing Fig. 6 and Fig. 9 the influence of cell rotations on the morphology of the monoclonal

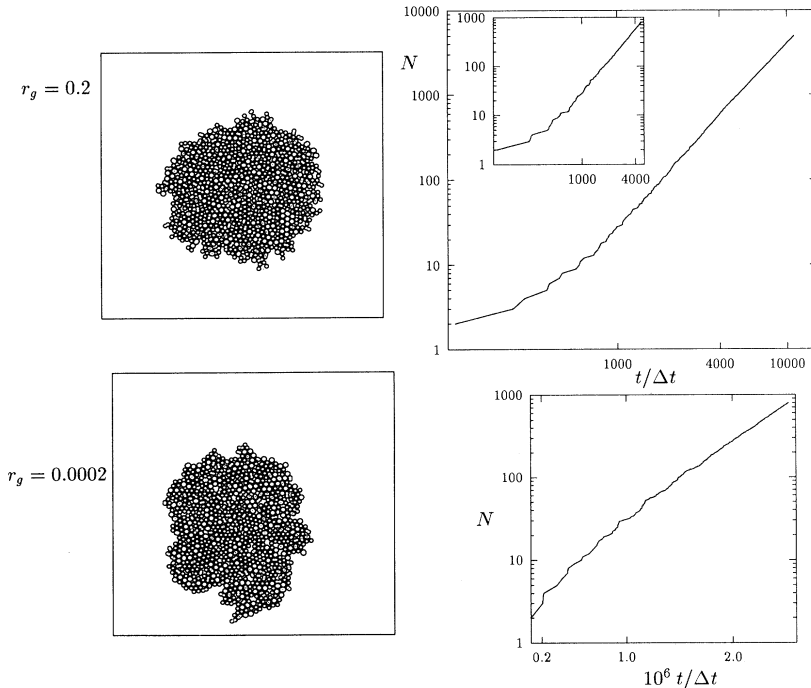


FIG. 6. Morphologies and growth law  $N(t)$  for strong attractive interaction ( $\epsilon = -20$ ). For  $r_g = 0.2$ , the growth law  $N(t)$  is plotted for populations of 800 cells (small picture) and of 5000 cells (large picture).

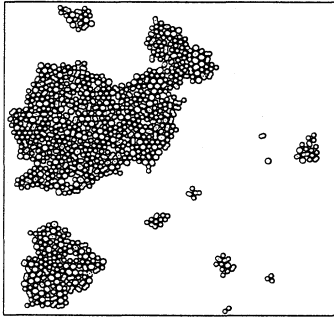


FIG. 7. Morphology for low growth rate  $r_g = 0.0002$  and intermediate attractive interaction ( $\epsilon = -5$ ).

can be studied. Note that without rotations cell clusters are considerably less spherical and contain larger internal holes than clusters of rotating cells. Noticeably these holes get even larger if the growth rate is reduced.

For  $t < t(800) < t_{cr}$ , the case of pure hard-core interaction resembles the above discussed noninteracting cell assemblies. However, as the growth rate increases, the cell assembly approaches a single spherical cluster with a power-law behavior of  $N(t) \sim t^\lambda$ . The exponent  $\lambda$  decreases with increasing  $r_g$  and reached  $\lambda \approx 2.53$  for our highest growth rate  $r_g = 0.2$ . The slowing down of cell growth from exponential to power law reflects the density regulation. With increasing density within the cell cluster more and more cells are prevented from proliferating by the contact inhibition due to the hard-core cell potentials. If only the  $\sim \sqrt{N}$  cells at the boundary of a compact cluster could proliferate one would expect  $\lambda = 2$  because in this case  $\Delta N \propto \sqrt{N} \Delta t$ . It seems, however, that there is a large time interval, where growth can be characterized by effective exponents considerably higher than 2, which depend continuously on the intrinsic growth rate. As we observed these exponents even in our longest simulation runs (up to 5000 cells; see, e.g., Fig. 6 for a simulation with the parameters  $r_g = 0.2$ ,  $\epsilon = -20$ ),

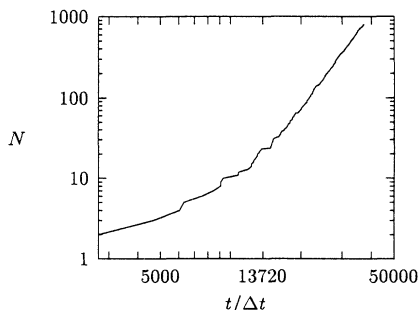


FIG. 8. Growth law  $N(t)$  for strong attractive interaction but intermediate growth rate. The estimated crossover time from Table I is  $t_{cr} \approx 13720$ .

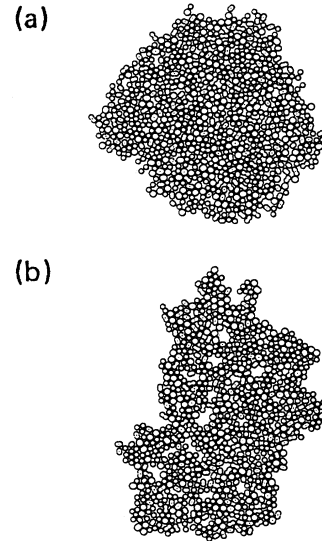


FIG. 9. Morphologies without cell rotation for  $\epsilon = -20$ . (a)  $r_g = 0.2$ , (b)  $r_g = 0.0002$ .

it is tempting to consider them as the asymptotic growth characteristics. Acceleration of growth beyond pure surface growth may result from an influx of free volume generated by the proliferation near the surface. At present we are performing much longer simulation runs to settle this question. But even the existence of a large transient regime characterized by effective power-law exponents is of interest for practical purposes as well as for further theoretical investigations.

As the attractive cell interaction is switched on and increased, the cell assembly shows a lesser tendency to disintegrate and for strong attraction ( $\epsilon = -20$ ) we observe only single cluster assemblies even for the lowest growth rates. Surprisingly, the crossover time is much less affected than one would expect from a simple estimate based on the average density within the cluster. For example, the average density of the clusters for  $\epsilon = -20$ ,  $r_g = 0.0002$  is  $\approx 0.8$  from the beginning of the growth process until  $t(800) \approx 1.6 \times 10^6 = 1.6t_0(800)$ . Nevertheless,  $N(t)$  follows an exponential law with  $\tau \approx 0.26 \times 10^6 = 1.88\tau_0$ , i.e., neither  $t(800)$  nor  $\tau$  deviate significantly from our naive estimates for noninteracting cells (although the morphology is drastically changed). We attribute this behavior to the fact that (although the cluster looks rather compact) there is enough time for free volume to diffuse across the entire assembly. After one growth step, the following 5000 migration trials (together with the rotation trials) are sufficient to reestablish the average cell distance (which is  $\delta/2$  for the square-well potential).

Although the cell assembly no longer disintegrates for strong attraction, we observe increasing boundary fluctuations and deviations from spherical cluster shape with decreasing growth rate (see Fig. 6). For moderately strong attraction we also observed disintegration into several clusters of variable size (Fig. 7). Typical cluster size

distributions are depicted in Fig. 10.

In a noninteracting assembly, the time  $t_0(800)$  is directly proportional to  $r_g^{-1}$ , i.e.,  $t_0(800) = m/r_g$  with  $m \approx 200$ . We find that even for interacting assemblies,  $t(800)$  scales approximately linearly with  $r_g^{-1}$ . The factor  $m$  increases with the strength of the attractive interaction:  $m(\epsilon = 0) \approx 248$ ,  $m(\epsilon = -2) \approx 250$ ,  $m(\epsilon = -5) \approx 300$ ,  $m(\epsilon = -20) \approx 500$ . This should only be taken as an empirical relation which may be of value for comparisons with experimental results.

The density and space-filling fraction profiles show plateaus of increasing length and sharper boundaries for pure surface growth (i.e.,  $\lambda$  close to 2) indicating compact cell clusters whereas the plateau length decreases with increasing  $\lambda$  until it vanishes completely and a boundary layer can no longer be defined (see Fig. 11).

The time evolution of cluster boundaries is depicted in Fig. 12. The boundaries of populations with 100, 200, ..., 800 cell individuals are shown. Note the increase of fluctuations for populations growing exponentially or with a power-law exponent  $\lambda$  larger than 2. Figure 12(c) shows the local roughness correlation function  $C(t(N = 100), t(N = k \times 100))$  which shows that clus-

ters growing exponentially or with  $\lambda > 2$  are strongly correlated with smaller ancestor clusters whereas clusters with pure surface growth tend to forget the shapes of their ancestors.

The boundary length  $\ell(\partial C)$  (as well as the mean cluster radius) scale according to

$$\ell(\partial C) \propto [M(C)]^{1/D} \quad (11)$$

with an exponent  $1/D \approx 0.53$  which is nearly independent of the growth rate for strong attraction ( $\epsilon = -20$ ). As  $1/D > 0.5$ , the clusters are not as compact as they seem from superficial inspection. In fact,  $2 - D$  controls the fraction of free volume in a cluster. Our statistics have not been sufficient until now to give reliable estimates of this quantity.

The mean number of interaction partners of a cell provides a good measure to distinguish compact cell clusters from disintegrated clusters consisting of only a few cells as can be seen from Fig. 13, where  $\bar{n}$  is plotted versus the logarithm of the growth rate  $r_g$ .

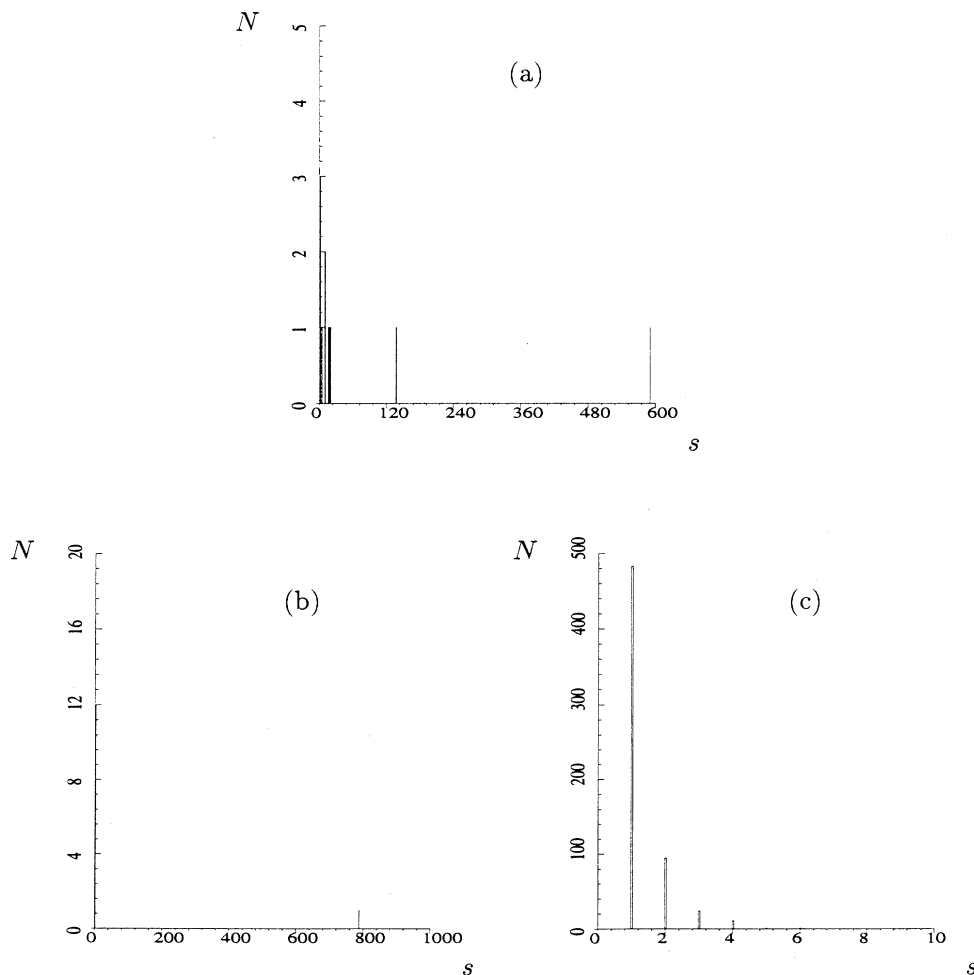


FIG. 10. Cluster size distribution, (a) for  $r_g = 0.0002$ ,  $\epsilon = -5$  (this corresponds to morphologies as shown in Fig. 7), (b) and (c) for pure hard-core interaction comparing (b) high growth rate  $r_g = 0.2$  and (c) low growth rate  $r_g = 0.0002$ .

### C. Internal properties of cells

Even for noninteracting cells, proliferation times are random and thus we expect to find nontrivial generation and age distributions. Fluctuations around the average generation number and age can be easily calculated exactly from first passage time distributions of one-dimensional random walks with one reflecting boundary (at  $R = R_{\min}$  for  $I$  cells and  $R = \zeta R_{\min}$  for  $M$  cells).

Figures 14 and 15 display generation number and age statistics. If  $t < t_{cr}$  we find exponential growth and a generation statistics which resembles that of noninteracting cells. Note that both the average generation number and the width of the distribution increase significantly if density regulation effects appear and the growth is slowing down to a power law. In Fig. 16 cells of specific generations are marked to show their distribution within the assembly. For high growth rates the cells of one generation form an almost concentric spherically symmetric ring, whereas they appear more and more scattered with decreasing  $r_g$ .

It is very interesting to study the statistics of subclones, i.e., the collection of cells with a common ancestor. Figure 17 shows the number of offspring  $N_k$  against the cell number  $k$ , where cells are numbered in chronological order of their first appearance. For noninteracting cells we expect  $N_k(t) = [N(t - t_k) - 1] = \exp(t - t_k) - 1$

with  $t_k$  denoting the time of appearance of cell number  $k$ . This curve is shown to fit the simulation data of exponentially growing interacting cell assemblies quite accurately (see Fig. 17). With increasing growth rate we observe strongly increasing fluctuations in the  $N_k$  as a function of cell number and the graphs are reminiscent of chaotic time series. Due to the strong contact inhibition of proliferation the production of offspring becomes increasingly complicated for a cell. Cell individuals which are located at or near the boundary and which have passed their cell cycle faster than the average have the highest probability to produce offspring. Once such a rare event occurs, it produces a cascade and it is the distribution of these offspring cascades which is reflected in the subclone morphologies of Figs. 18 and 19.

The blocking effects of density regulation also leads to an increase of the average interphase-mitosis time ratio  $f^{IM}$  by a factor of  $\approx 3$ . We found no dependence of this enhancement on the ratio we chose for the isolated cell. It should be noted, however, that the distribution of the ages of  $M$  cells is very inhomogeneous within the clusters and therefore the average  $f^{IM}$  is not a typical quantity for cells in compact clusters.

Tables II and III summarize growth characteristics for cells with interaction ranges which we considered to be plausible for epithelial cells in culture. The basic time scales are given in units of the corresponding noninteracting population from Table I, i.e.,

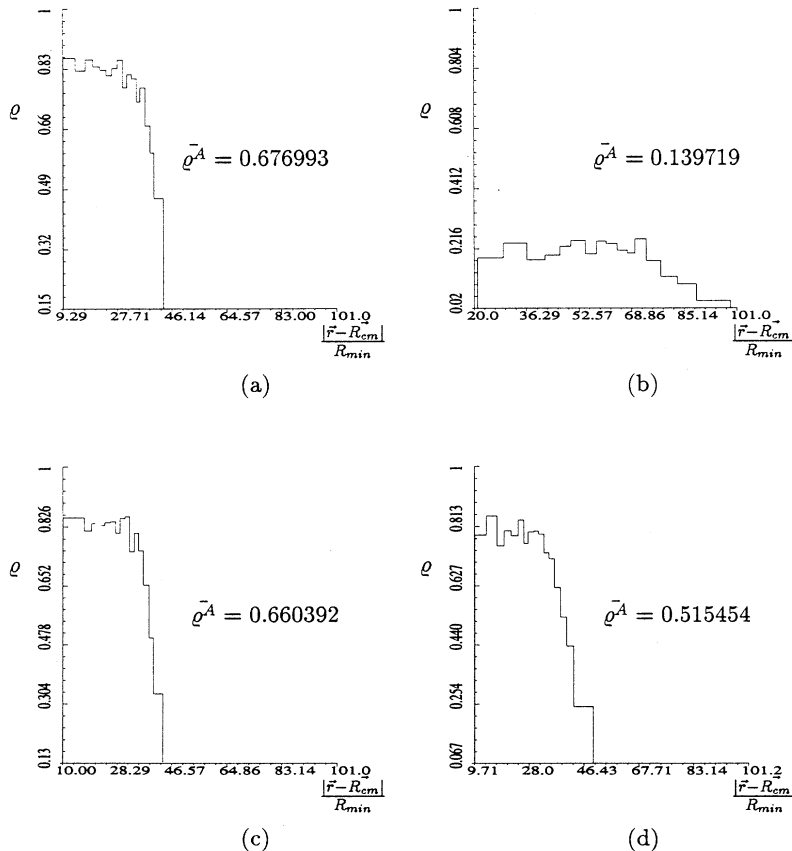


FIG. 11. Area filling profile (a) and (b) for pure hard-core potential and  $r_g = 0.2$  (a),  $r_g = 0.0002$  (b) (see Fig. 8), and (c) and (d) for strong attraction  $\epsilon = -20$  and  $r_g = 0.2$  (c),  $r_g = 0.0002$  (d).

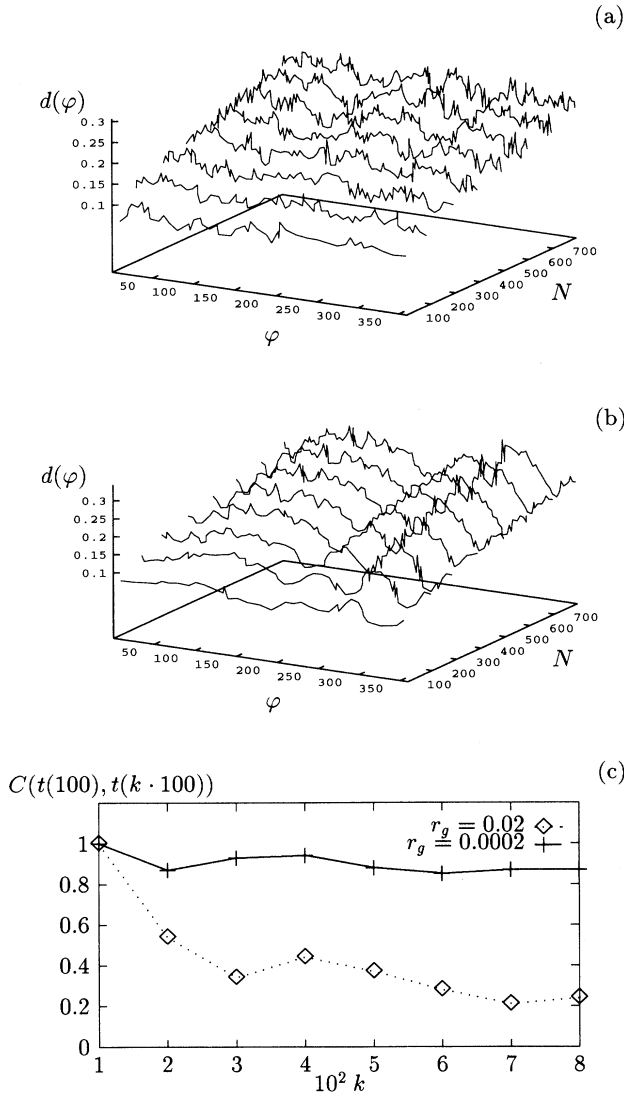


FIG. 12. Temporal development of cell cluster boundary [ $\epsilon = -20$ ,  $r_g = 0.2$  (a),  $r_g = 0.0002$  (b)] and local roughness correlation for the boundaries (c).

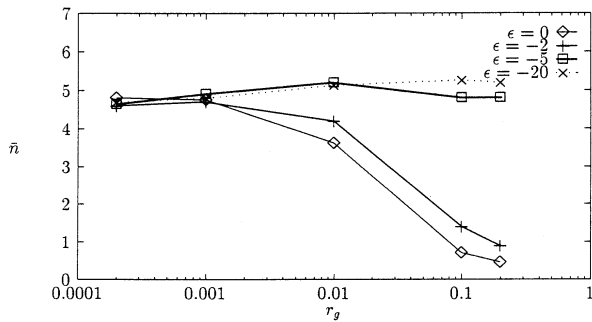


FIG. 13. Average number of interaction partners  $\bar{n}$  versus growth rate (logarithmic scale).

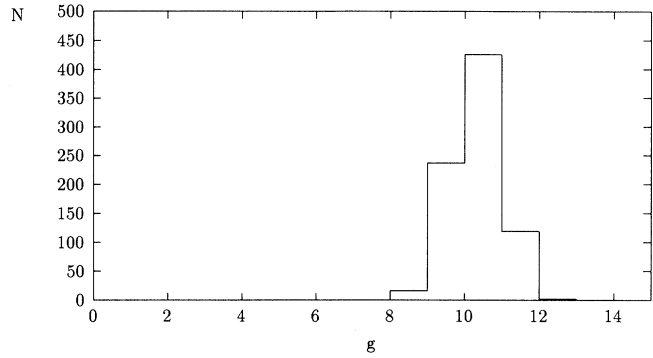


FIG. 14. Generation number statistics for  $\epsilon = 0$  and  $r_g = 0.0002$  ( $N$ , number of cells;  $g$ , generation number). This form is very similar to the generation number statistics of noninteracting cells.

$$T_f = t_{\text{interact}}(800)/t_0(800), \quad (12)$$

$$\tau = \tau_{\text{interact}}/\tau_0.$$

D. Variants of the basic model

The global growth characteristics of models *B* and *C* are collected in Tables IV and V. Figures 20 and 21 dis-

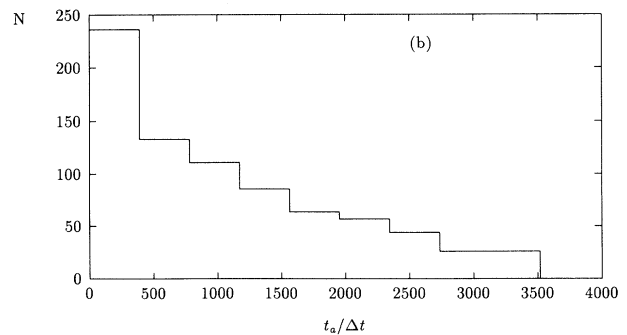
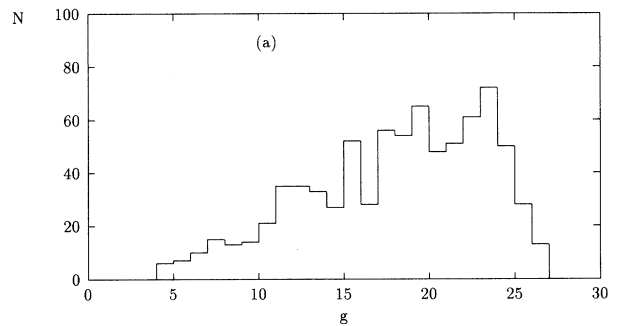


FIG. 15. Generation number statistics (a) and corresponding age distribution (b) for  $\epsilon = -20$ ,  $r_g = 0.2$ .  $t_a$  denotes the age.

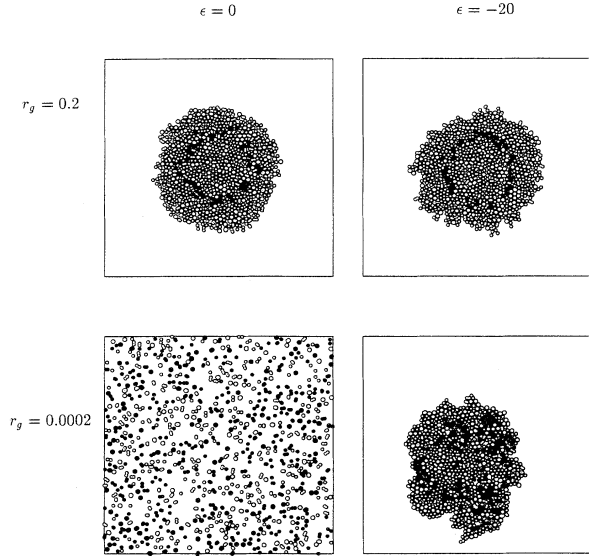


FIG. 16. Morphologies of special generations (marked in black). For  $r_g = 0.0002$  the 10th generation is marked. For  $r_g = 0.2$  it is the 12th generation for  $\epsilon = 0$  and the 15th generation for  $\epsilon = -20$ .

TABLE II. Growth characteristics of 800 cell monoclones generated by model A. See Eq. (12) for the definition of  $\tau$  and  $T_f$ .  $\lambda$  denotes the exponent of power-law growth of  $N(t)$ .  $\bar{g}$  is the mean generation number. x denotes values that represent neither a power law nor an exponential, dashes denote values that cannot be defined because the growth cannot obey a power law as well as an exponential at the same time.

$r_g$	$T_f$	$\tau$	$\lambda$	$\bar{g} (\pm \Delta g)$
$\epsilon = 0$				
0.2	2.63	-	2.61	13.8 ( $\pm 3.6$ )
0.1	2.06	-	2.73	11.9 ( $\pm 2.6$ )
0.01	1.29	x	x	9.84 ( $\pm 0.8$ )
0.001	1.26	1.2	-	9.80 ( $\pm 0.7$ )
0.0002	1.15	1.2	-	9.80 ( $\pm 0.7$ )
$\epsilon = -2$				
0.2	3.90	-	1.98	16.2 ( $\pm 4.8$ )
0.1	3.27	-	2.46	14.8 ( $\pm 4.0$ )
0.01	1.62	-	3.50	10.2 ( $\pm 1.4$ )
0.001	1.18	1.3	-	9.8 ( $\pm 0.7$ )
0.0002	1.17	1.2	-	9.8 ( $\pm 0.8$ )
$\epsilon = -5$				
0.2	4.67	-	2.10	17.0 ( $\pm 5.2$ )
0.1	3.88	-	2.28	15.5 ( $\pm 4.4$ )
0.01	2.86	-	2.60	11.8 ( $\pm 2.6$ )
0.001	1.95	x	x	10.2 ( $\pm 1.3$ )
0.0002	2.00	x	x	10.7 ( $\pm 2.0$ )
$\epsilon = -20$				
0.2	4.68	-	2.03	17.6 ( $\pm 5.3$ )
0.1	4.01	-	2.30	15.5 ( $\pm 4.6$ )
0.01	2.93	-	2.25	11.8 ( $\pm 2.6$ )
0.001	2.55	x	x	10.4 ( $\pm 1.6$ )
0.0002	2.53	x	x	10.4 ( $\pm 1.6$ )

TABLE III. Growth characteristics for 800 cell monoclones with interactions of longer range with  $\epsilon = -20$  and  $\delta = 0.5R_{\min}$  generated by model A. For the definition of  $\tau$ ,  $T_f$ , and  $\lambda$  (see Table I),  $\bar{g}$  is the mean generation number.

$r_g$	$T_f$	$\tau$	$\lambda$	$\bar{g} (\pm \Delta g)$
0.2	3.24	-	2.20	14.9 ( $\pm 4.3$ )
0.1	2.72	-	2.60	13.3 ( $\pm 3.3$ )
0.01	1.86	-	3.50	10.5 ( $\pm 1.7$ )
0.001	1.62	2.00	-	10.1 ( $\pm 1.1$ )
0.0002	1.60	1.88	-	10.1 ( $\pm 1.2$ )

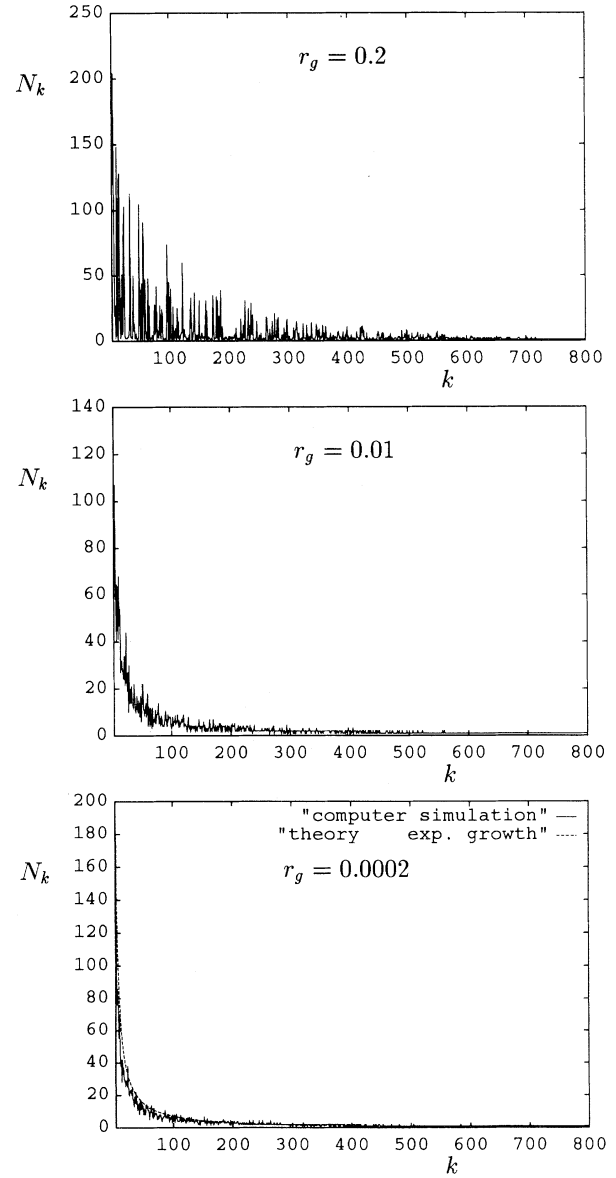


FIG. 17. Number of offspring  $N_k$  of cell number  $k$  (cells are numbered in chronological order). The dotted line shows the result for a simple exponential growth law ( $\epsilon = 0$ ).

TABLE IV. Growth characteristics of 800 cell monoclonal for  $\epsilon = -20$  and model *B*. For the definition of  $\tau$ ,  $T_f$ , and  $\lambda$  (see Table I),  $\bar{g}$  is the mean generation number.

$r_g$	$T_f$	$\tau$	$\lambda$	$\bar{g} (\pm \Delta g)$
0.2	3.34	–	2.3	14.5 ( $\pm 4.0$ )
0.1	2.65	–	2.5	13.0 ( $\pm 3.2$ )
0.01	1.60	–	4.2	10.0 ( $\pm 1.1$ )
0.001	1.33	1.49	–	9.8 ( $\pm 0.7$ )
0.0002	1.38	1.49	–	9.8 ( $\pm 0.66$ )

play pictures of the morphologies. For fixed growth rate, the variants produce less compact clusters than the basic model as should be expected from the lack of adhesion during the *M* phase. For the same reason *I* cells appear more clustered than *M* cells. For low growth rates, the cluster statistics of *I* and *M* cells are completely different. More and more single *M* cells appear which dissociate from the boundaries of small or medium sized *I* cell clusters. Figure 22 shows the average number of clusters versus  $r_g$  for models *A, B, C*. For growth rates larger than  $\approx 0.01$  the differences between models *A, B, and C*

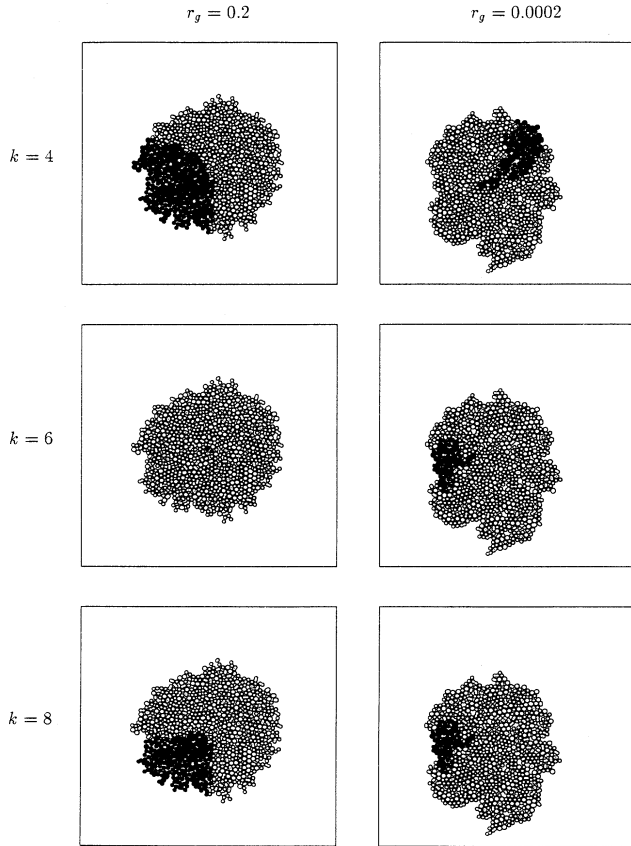


FIG. 18. Subclone morphologies. The offspring of one cell is marked in black.

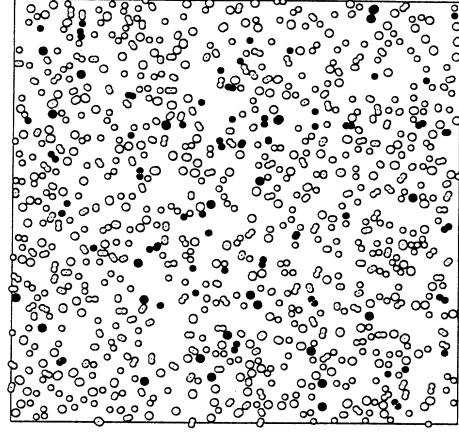


FIG. 19. Subclone morphology of cell number  $k = 6$  for  $\epsilon = 0$  and  $r_g = 0.0002$ .

population gradually become less significant.

Table VI shows the characteristics of cell growth after the inclusion of cell death (model *D*). Figure 23 displays some typical morphologies. Note that the total number of clusters remains quite small and decreases with decreasing  $r_g$  (in contrast with models *B* and *C*). Nevertheless, the density fluctuations are very large due to the fractal structure of cell clusters. As one approaches  $p_D = 1$ , fluctuations on all length and time scales start to grow (see Fig. 24 and Fig. 25). We would like to stress that the effects of cell death *cannot* be taken into account by a simple rescaling of the basic replication rate. In an interaction free cell assembly, cell death will lead to a prolongation of  $\tau_0$ ,

$$\tau_0(p_D) = \tau_0 \frac{\ln 2}{\ln(2 - p_D)}. \quad (13)$$

In Table VI the times  $T_f$  and  $\tau(p_D)$  are given in units of the rescaled times, i.e.,

$$T_f(p_D) := \frac{t_{\text{interact}}(800, p_D) \ln(2 - p_D)}{t_0(800) \ln 2}, \quad (14)$$

$$\tau(p_D) := \tau_{\text{interact}}(p_D) / \tau_0(p_D).$$

For interacting populations, our cell death mechanism also affects the density regulation by creating free volume at a rate proportional to the number of replicating cells.

TABLE V. Growth characteristics of 800 cell monoclonal for  $\epsilon = -20$  and model *C*. For the definition of  $\bar{c}$ ,  $T_f$ , and  $\lambda$  see Table I.

$r_g$	$T_f$	$\tau$	$\lambda$	$\bar{g} (\pm \Delta g)$
0.2	5.11	–	2.0	18.9 ( $\pm 6.2$ )
0.1	4.10	–	2.2	16.4 ( $\pm 4.8$ )
0.01	1.99	–	3.0	11.2 ( $\pm 2.3$ )
0.001	1.49	1.55	–	9.9 ( $\pm 1.0$ )
0.0002	1.33	1.62	–	9.8 ( $\pm 0.7$ )

**IV. SIMULATING BIOLOGICAL PROCESSES IN TISSUE**

Up to now, we have concentrated on the study of some basic models for tissue cell growth which by themselves cannot be considered as realistic *in vivo*. Nevertheless, they displayed a variety of salient features which may be confronted with cell culture experiments. We consider these studies as necessary prerequisites for investigations of more specific biological situations. Although it is not the main point of this work to consider any such situations in detail, we present some results for two interesting processes of tissue cell biology: the growth of a sarcoma across an epithelial boundary and the regeneration of a skin cut. We will discuss these processes without any further refinement of our models. Due to our restriction to quasi-two-dimensional systems, we cannot hope for much more than an analogy of these processes. Nevertheless we found it a worthwhile exercise because on the one hand the restriction to two dimensions is easily released while on the other hand even the two-dimensional systems display some very illuminating features of the modeled biological scenarios. Our main motivation for studying these surely oversimplified descriptions of cells is to separate *collective* phenomena in assemblies of cells,

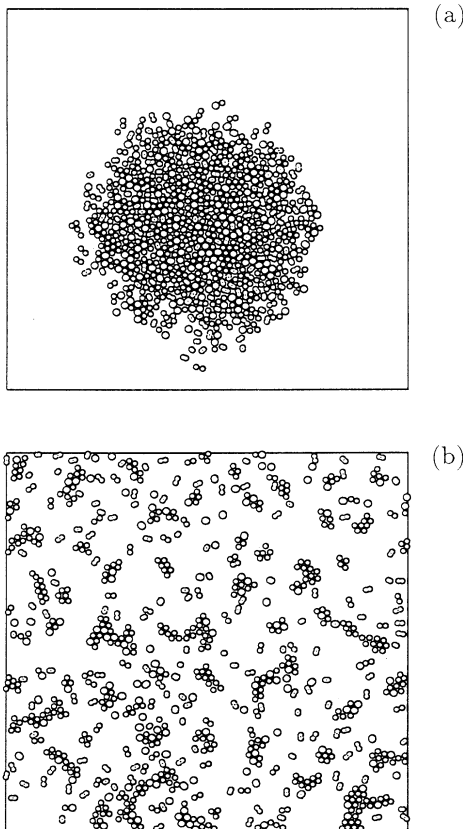


FIG. 20. Morphologies of model *B* for  $\epsilon = -20$ . (a)  $r_g = 0.01$ , (b)  $r_g = 0.0002$ .

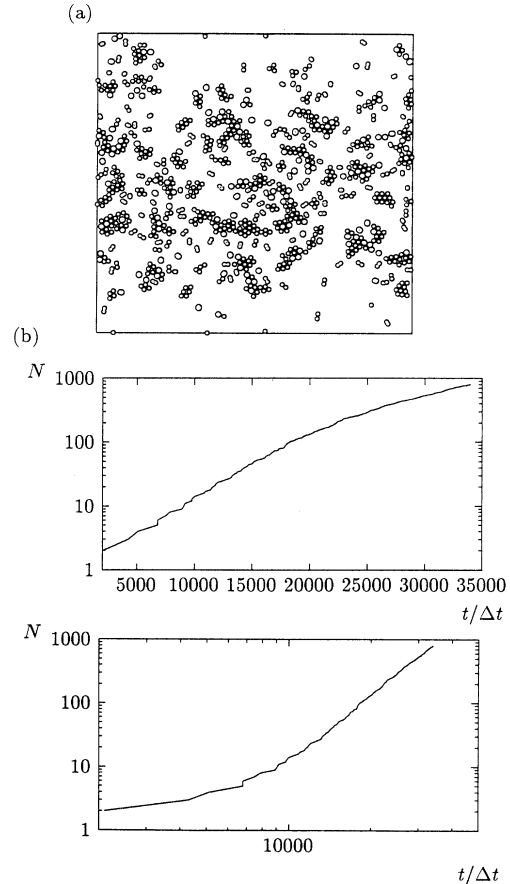


FIG. 21. (a) Morphology of model *C* for  $\epsilon = -20$  and  $r_g = 0.0002$ . (b) Growth law  $N(t)$  for model *C* displaying crossover from exponential to power law ( $\epsilon = -20, r_g = 0.01$ ). The estimated crossover time  $t_{cr}$  (see Table I) is  $t_{cr} \approx 13\,720$ .

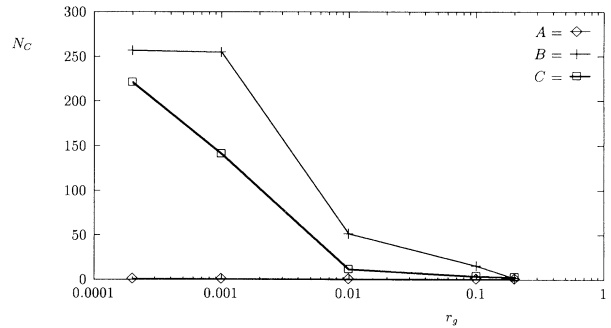


FIG. 22. Average number of clusters versus growth rate for models *A, B, C*.

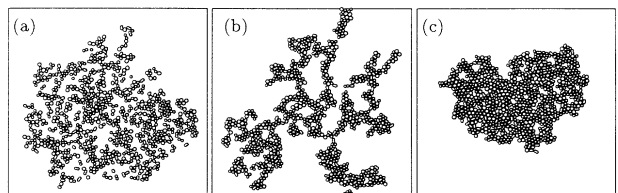


FIG. 23. Morphologies of model *D* for  $\epsilon = -20$ . (a)  $r_g = 0.0002, p_D = 0.5$ ; (b)  $r_g = 0.0002, p_D = 0.95$ ; (c)  $r_g = 0.2, p_D = 0.95$ .

each with fixed and simple properties, from *genetically regulated* phenomena which depend on the intrinsic cell dynamics in a complicated way. We believe that a better understanding of the interplay between these two regulation mechanisms is important for the development of a theory of pattern formation and cell differentiation in living organisms. A more detailed presentation of this part of our work can be found in [56,60].

### A. Sarcoma growth across epithelial boundaries

A sarcoma is a malignant tumor of the connective tissue. The proliferating tumor cells excrete collagenase which digests the intercellular contacts in the epithelial structures (e.g., [61]). We consider a two-dimensional analogy of this situation by starting out from a single tumor cell surrounded by a layer of model *F* cells which form a stable circular ring. After some time, the growing tumor will fill up all of the space within the circular cavity and reach the epithelial boundary. We assume

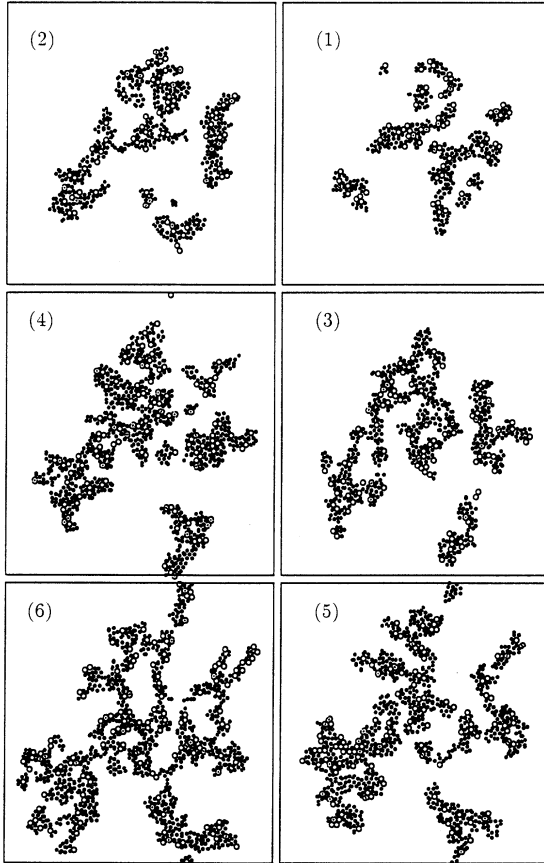


FIG. 24. Temporal development of morphologies of model *D* near criticality ( $r_g = 0.0002$ ,  $p_D = 0.95$ ). Note that cell clusters disintegrate and reaggregate on large scales. The first picture displays 300 cells, the last one 800.

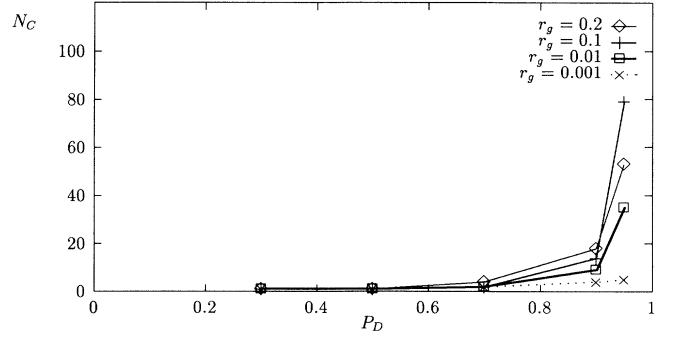


FIG. 25. Average number of clusters versus  $p_D$  of model *D*.

that the attractive interaction between epithelial cells is much stronger than between tumor cells and there is no attractive interaction between cells of different type (e.g., [62–65,53]). (We chose potential minima  $\epsilon = -20$  for epithelial and  $\epsilon = -2$  for tumor cells.) Both cell types were assumed to be of the same size  $R_{\min}$  and the range of interactions was taken to be  $\delta = 0.2R_{\min}$ .

For attractive potentials of the square-well type the

TABLE VI. Growth characteristics of 800 cell monoclones including cell death for  $\epsilon = -20$ . For the definition of  $\tau(p_D)$  and  $T_f(p_D)$  see Eq. (14).  $p_D$  is the probability for a cell to be killed (see Sec. II C, Model *D*),  $\bar{g}$  is the mean generation number and  $\lambda$  denotes the exponent of power-law growth of  $N(t)$ .

$r_g$	$T_f(p_D)$	$\tau(p_D)$	$\lambda$	$\bar{g} (\pm \Delta g)$
$p_D=0.3$				
0.2	3.80	–	2.36	20.3 ( $\pm 5.1$ )
0.1	3.60	–	x.xx	20.7 ( $\pm 4.4$ )
0.01	2.96	–	3.57	16.6 ( $\pm 2.5$ )
0.001	2.67	–	4.0	15.3 ( $\pm 1.7$ )
$p_D=0.5$				
0.2	3.40	–	2.4	24.6 ( $\pm 5.1$ )
0.1	3.32	–	3.0	26.7 ( $\pm 4.6$ )
0.01	2.82	–	3.64	22.1 ( $\pm 3.0$ )
0.001	2.80	–	5.3	24.1 ( $\pm 1.9$ )
$p_D=0.7$				
0.2	3.10	–	2.9	39.8 ( $\pm 4.3$ )
0.1	2.87	–	3.7	37.0 ( $\pm 4.2$ )
0.01	2.78	–	4.2	33.7 ( $\pm 3.0$ )
0.001	3.00	–	5.9	44.3 ( $\pm 2.0$ )
$p_D=0.9$				
0.2	2.95	–	5	133.9 ( $\pm 5.1$ )
0.1	2.63	–	5	114.0 ( $\pm 4.0$ )
0.01	2.23	3.17	–	94.8 ( $\pm 4.0$ )
0.001	2.75	4.09	–	115.2 ( $\pm 4.6$ )
$p_D=0.95$				
0.2	2.33	3.14	–	199.2 ( $\pm 4.8$ )
0.1	2.31	2.76	–	210.0 ( $\pm 4.2$ )
0.01	2.42	2.72	–	200.0 ( $\pm 4.9$ )
0.001	2.84	4.12	–	189.0 ( $\pm 5.5$ )

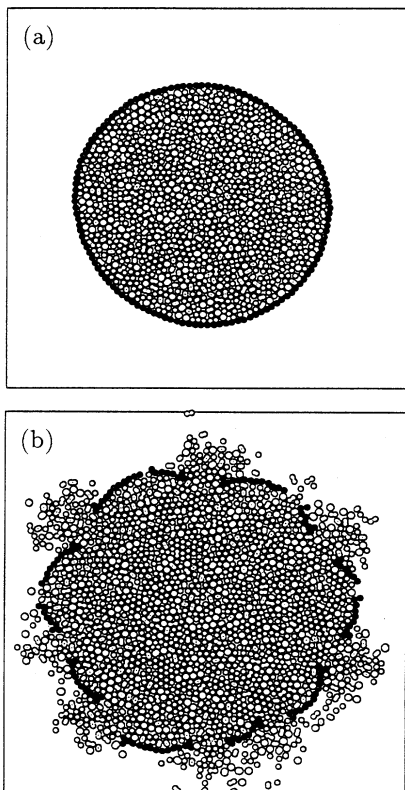


FIG. 26. Morphologies of model sarcoma confined by an epithelial barrier. (a) Square-well potential between epithelia cells. The tumor remains confined. (b) If the potential is softened to a harmonic well of the same depth (by secreted collagenase of tumor cells) the epithelial barrier is overrun (model parameter as described in the text).

tumor always remained confined within the cavity (Fig. 26). We may model the influence of the secreted collagenase by a softening of the potential from a square well to a harmonic well. In fact, if the potential is smoothed to a harmonic well (see Fig. 4) of the same depth as the square well, we observe that the growing tumor overruns the epithelial barrier. Figure 27 shows the growth law

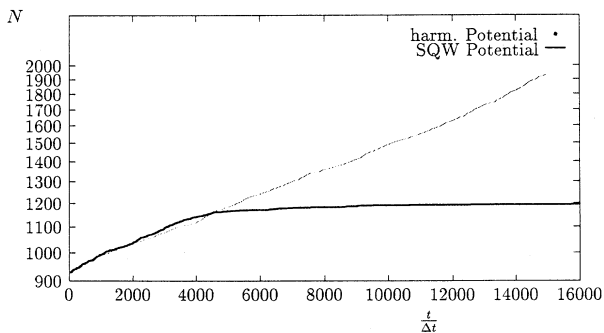


FIG. 27. Growth laws  $N(t)$  for the two situations depicted in Fig. 27.

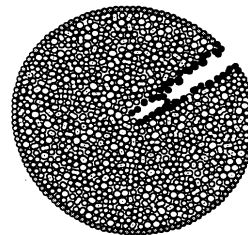


FIG. 28. Model of a skin cut. The outer layer consists of model  $F$  cells, the interior of model  $D$  cells. Cells which are marked black switch into proliferation metabolism due to a lack of neighbors.

for these two types of potentials. Note that the epithelial layer is broken only at a few spots but each spot is the starting point of an exponentially growing cascade.

### B. Wound healing of a skin cut

Suppose now that we have a similar situation as indicated in Fig. 26(a) but the cells filling up the spherical cavity are not tumor cells but differentiated connective tissue cells (fibroblasts), i.e., they are not proliferating. We simply consider them as an assembly of model  $E$  cells. Assume now that we cut out a part of the cells in a sector as indicated in Fig. 28. This situation constitutes our analog of a skin cut. Due to the lack of neighbors, the cells at the boundary of the cut switch into the proliferating state (see Sec. II C) and begin to refill the cut with tissue material.

Let us discuss the process of wound healing from a more biological point of view to clarify that our model does not contain unplausible assumptions although it

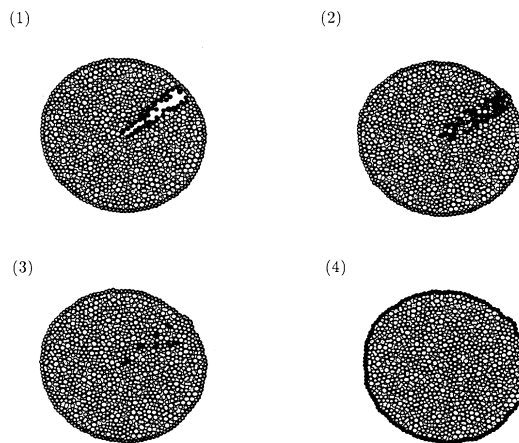


FIG. 29. Steps of the wound healing process. Note that finally all cells have switched back into nonproliferating tissue cells. We used the regulation criterion (b) of model  $E$ , i.e., cells are switched back into nonproliferating state if their growth velocity becomes too small.

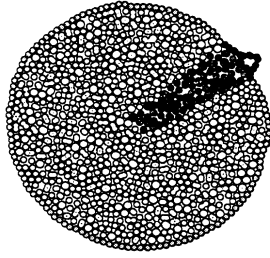


FIG. 30. If cells do not switch back into nonproliferating state properly due to disturbances of the regulation mechanism, the wound develops a macroscopically distorted scar.

strongly simplifies the regeneration process. Histologically, one may distinguish between four phases which we roughly characterize as follows.

(a) *Exsudative phase*. Macrophages and thrombocytes enter the wound from hurt blood vessels. They start the clotting cascade by aggregating at collagen fibers.

(b) *Resorptive phase*. Cells of the immune system (neutrophil granulocytes, monocytes, and lymphocytes) migrate into the wound. They kill invading bacteria and take up tissue remains and dead cells. The secreted decomposition products serve as nutrients for the fibroblasts in the next phase.

(c) *Proliferating phase*. Macrophages and thrombocytes release growth factors which stimulate the proliferation of fibroblasts and epithelial cells at the edge of the cut. The growing and proliferating cells fill the cut with granulation tissue.

(d) *Repair phase*. The granulation tissue is replaced by denser scar tissue and epithelial cells form a new epithelial boundary which finally stops proliferating by contact inhibition.

Note that although the switching of fibroblasts and epithelial cells into the proliferating state is accomplished by a mechanism which is different from that in model *E*, the result is the same: cells at the boundary of the cut begin to proliferate. Our model thus seems adequate for the description of the last two phases of wound healing.

In Fig. 29 we show a sequence of morphologies during the regeneration process which correctly restores the original macroscopic pattern. Both regulation criteria of model *E* which were introduced to switch back from proliferation to tissue function lead to a satisfying restoration of the original macroscopic structure. Figure 30 displays what happens if cells do not stop proliferating due to disturbances of the regulation mechanism. The resulting form of the epithelial layer is reminiscent of a macroscopically distorted scar.

## V. DISCUSSION AND OUTLOOK

In the present work we have developed a stochastic model for growing populations of tissue cells with special emphasis on epithelial cells and cells of the connec-

tive tissue. We studied applications of the basic model and several biologically motivated variants by performing Monte Carlo simulations of monoclonal growth in culture. Figure 31 summarizes the explored regions of

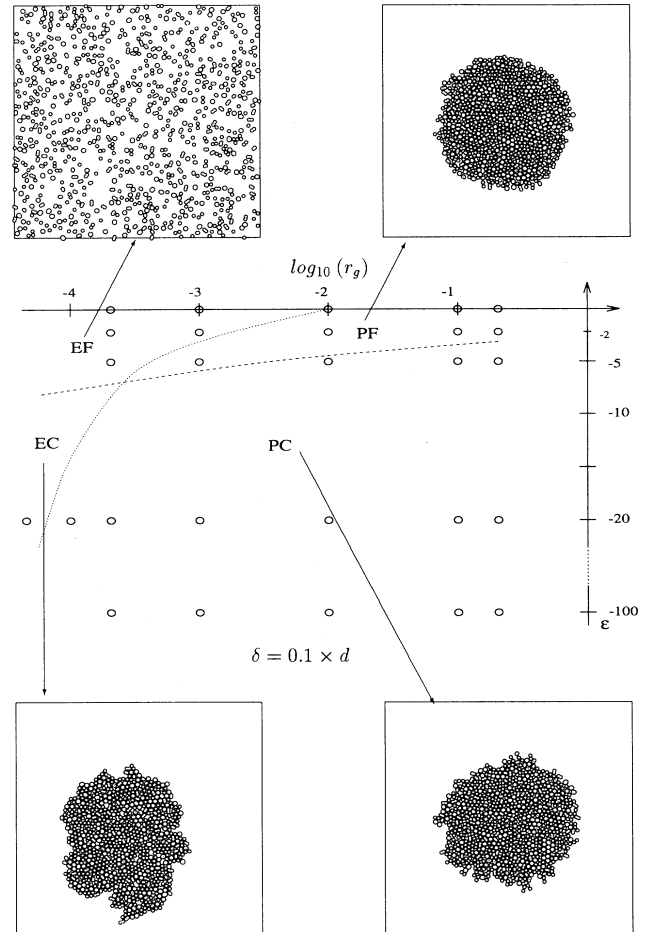


FIG. 31. Two-dimensional projection  $(\log_{10}(r_g), \epsilon)$  of the three-dimensional parameter space  $(\log_{10}(r_g), \epsilon, \delta)$  for simulations up to 800 cells with fixed  $\delta = 0.2R_{\min} = 0.1d$  ( $d$  is the cell diameter). The small circles denote the parameter combinations used in the computer simulations. Four different regions with qualitatively different behavior have been found (for each of the regions, a pointer is drawn to the corresponding morphology of the population). For weak attraction and a small growth rate, exponential growth has been found (EF); for weak attraction and a high growth rate, we find a power law for the population growth (PF); for strong attraction and high growth rate, the population growth is again due to a power law, but here, all cells belong to the same cluster (PC); and for strong attraction and low growth law we find an exponential growth law where, again, all cells belong to the same cluster (EC). The dashed line shows the border between populations, which all belong to the same cluster (EC and PC) and populations, which do not (EF and PF); the dashed-dotted line marks the border between exponential growth (EC and EF) and growth due to a power law (PC and PF).

growth rate and cell interaction strength and depicts the corresponding growth laws. Furthermore we considered two-dimensional analogies of more complex processes: the growth of a sarcoma across an epithelial boundary and the wound healing of a skin cut.

Although we only performed simulations for two dimensional systems (which seems adequate for cell culture experiments) the models and the developed algorithms can be used for three-dimensional tissues as well. The state space for rotation for a cell in three dimensions has to be increased by a further angle variable and the MC step for rotation effects both azimuthal and polar angle.

Once the basic time scale  $\Delta t$  and the ratio  $f^{IM}$  of the average durations of  $I$  and  $M$  phase have been fitted to the migration of a single cell, our results can in principle be confronted with quantitative experiments. We conclude from our simulations that in order to produce the observed value of the interphase-mitosis time ratio of cell cycles in tissue ( $\approx 12$ –25),  $f^{IM}$  must be  $\approx 4$ –8. We did not succeed in finding reliable data for *single cells* in the literature. This, however, is not the only reason for us to refrain for postponing detailed comparisons of the present work with experimental data. Before we do this, we must be aware that tissue cells do not live in free space (as we have assumed in our models) and that the structure of the extra-cellular medium may have profound influences on growth and pattern formation. To overcome this incompleteness of our description, we are currently adding a cell-substrate interaction to our basic model. Such interactions result from substrate-adhesion molecules [44] and lead to *haptotaxis*, i.e., a dependence of cell mobility on the properties of the extra-cellular medium [48,26]. Nevertheless, we believe that even the simplest version of our model without cell-substrate interactions already captures a lot of salient features of tissue cell growth.

As it is possible to influence both the intrinsic growth rate of cells in culture (via the cell metabolism) and the strength of their attractive interaction (via appropriate CAM antibodies [48]), it may become possible to observe the crossover scenarios from high to low growth rates and from strong adhesion to pure cell repulsion which we described in Sec. III. If the simulation results could be appropriately calibrated, it may even become possible to use Monte Carlo simulations for medical diagnostic purposes.

In this respect it is of particular interest to try to model the dedifferentiation and deadaptation effects which are shown by normal tissue cells in culture. For example, normal tissue cells often produce clones of immortal cells in culture [66]. Thus it is not possible to distinguish such clones from clones of malignant tumor cells on the basis of cell mortality. Nevertheless the growth characteristics of normal and tumor cell clones should be different, because the normal cells have to learn immortality via the selection pressure within the culture substrate.

Section IV contains our starting point for a theoretical understanding of tissue *in vivo*. A necessary refinement is the inclusion of long-range interactions via secreted biological transmitters. In living organisms, this type of interaction is responsible for a variety of subtle regulation mechanisms which lead to different behavior of cells in

culture and in differentiated tissue *in vivo*.

Within our model, we have studied various interaction ranges leading to results which are at least qualitatively identical to those obtained with  $\delta = 0.2R_{\min}$ . (Quantitative differences may be estimated from Tables II and III.) For  $\delta \ll R_{\min}$  we have found no significant deviations. For  $\delta = R_{\min}$ , however, we already observed qualitatively new phenomena. As an example, Fig. 32 shows the average number of generations necessary to create an 800 cell monoclonal versus the growth rate for three different interaction ranges. Whereas for short-range interactions  $\bar{g}$  decreases monotonically with  $r_g$  and approaches the value for noninteracting cells, it shows a pronounced minimum and a sharp rise towards lower growth rates for  $\delta = R_{\min}$ . In Fig. 33 we show the regions of the interaction range  $\delta$  which we have systematically explored together with the corresponding growth laws.

In conclusion, we have shown that a Monte Carlo approach to populations of tissue cells is an effective modeling strategy and leads to interesting results which in principle can be compared with experiments on cell cultures. It is capable of bridging the gap between rate equation (or more elaborate reaction-diffusion equation) approaches, which focus on macroscopic pattern formation, and the histological models of single cells.

In the present work, we have considered only the simplest histological properties. Due to the statistical description of cell shapes our model cells therefore resemble spherical and nonspherical molecules with autocatalytic reactions. In fact, the proposed algorithm provides sample trajectories of a master equation which can be interpreted as an autocatalytical reaction scheme [67]. With the inclusion of more and more specific biological mechanisms and processes (like those indicated in Sec. IV), however, the analogy to systems of molecules fades away while at the same time analytical results are increasingly complicated to obtain. Simulations, on the other hand, can be refined without much effort. Such further refinements may perhaps even lead to models applicable to the tissue of living organisms in the future.

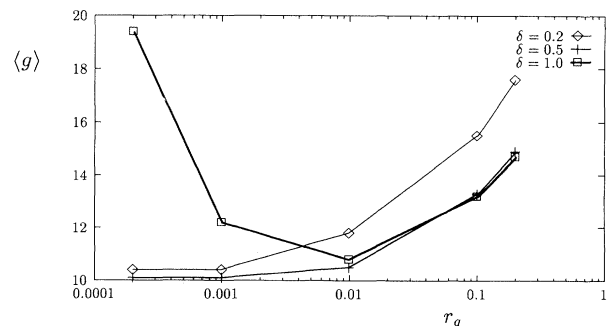


FIG. 32. Average number of generations in an 800 cell monoclonal for different interaction ranges.

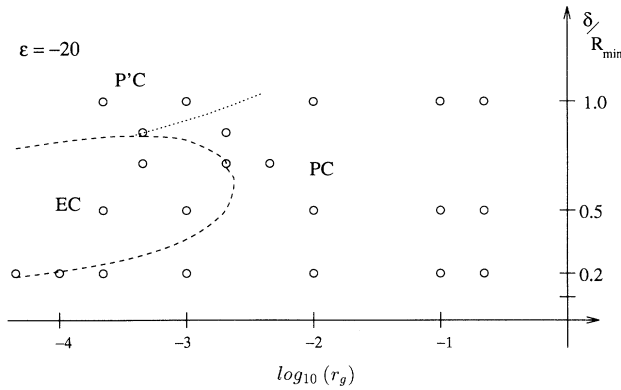


FIG. 33. Two-dimensional projection ( $\log_{10}(r_g), \delta$ ) of the three-dimensional parameter space for simulations up to 800 cells with fixed  $\epsilon = -20$ . In the regime PC we found a power law for the growth, with increasing exponent as  $r_g$  decreases. In the regime EC we found exponential growth, the dashed line denotes approximately the border between the regimes PC and EC. For small growth rates and high interaction ranges, we again found a power law for the grow (PC), probably due to interaction between next-nearest neighbors (here, the average number of interaction partners for cells in the inner of a cluster becomes larger than six).

#### ACKNOWLEDGMENTS

One of the authors (D.D.) wants to thank Manfred Eigen for technical support and the Institut for Biotechnology in Jena for financial support.

#### APPENDIX: SIMULATION ALGORITHM

This appendix gives a brief description of the Monte Carlo algorithm of the basic model. A flow chart is shown in Fig. 34. Every updating step starts with a random choice of one of the cells of the assembly which is switched into an active state (CHOOSECELL). The second step consists in choosing the special trial (CHOOSE TRIAL). CHOOSE TRIAL may be realized in two ways. In the first case, there are internal counters for each action which are enhanced by 1 whenever the corresponding action is performed. Trials of a certain activity are performed until the counter has reached a maximum value. Then the updating switches to the next most frequent type of activity. In this way there are  $\nu_{\text{rot}}$  rotation trials (on  $\nu_{\text{rot}}$  different randomly chosen cells) before the next migration trial is performed, etc. In the second algorithm, a trial is chosen randomly but with unequal probabilities such that the frequencies of rotation, migration, and growth-deformation are distributed in the proportions  $\nu_{\text{rot}}:\nu_{\text{mig}}:\nu_{\text{growth}}$ .

During each of the activities ROTATE, MIGRATE, GROW, DEFORM a random choice is made among all the possible trials of one type. Afterwards this trial is ac-

cepted or rejected on the basis of the change in interaction potential which it implies. To simplify the notation we will leave out the subscript of the chosen cell below. RAND denotes a random number drawn from the interval  $[0,1]$ .

MIGRATE:

$$\vec{r}(n+1) = \vec{r}(n) + \eta \delta \vec{r}. \quad (\text{A1})$$

$\delta \vec{r}$  is a random shift drawn from all the vectors which are equally distributed within a circle of radius  $\delta r_{\text{max}}$ . The binary variable  $\eta = 1$  (i.e., the trial is accepted) if  $\text{RAND} \leq \exp(-\Delta E_{\text{mig}})$  and  $\eta = 0$  otherwise. This is the usual Metropolis prescription.  $\Delta E_{\text{mig}}$  denotes the change in the potential (which controls migration) due to the trial.

GROWTH:

$$\hat{R}(n+1) = R(n) + \eta \delta R. \quad (\text{A2})$$

Again  $\eta = 1$  if  $\text{RAND} \leq \exp(-\Delta E_{\text{growth}})$ . If  $\hat{R}(n+1) \leq R_{\text{max}} = \zeta R_{\text{min}}$ , then  $R(n+1) = \hat{R}(n+1)$ . Otherwise  $R(n+1) = R_{\text{max}}$ . The random number  $\delta R$  is drawn from the equally distributed reals within the interval  $[0, \delta R_{\text{max}}]$ . As  $E_{\text{growth}}$  only consists of the hard-core potential in the basic model, the Metropolis prescription amounts to a

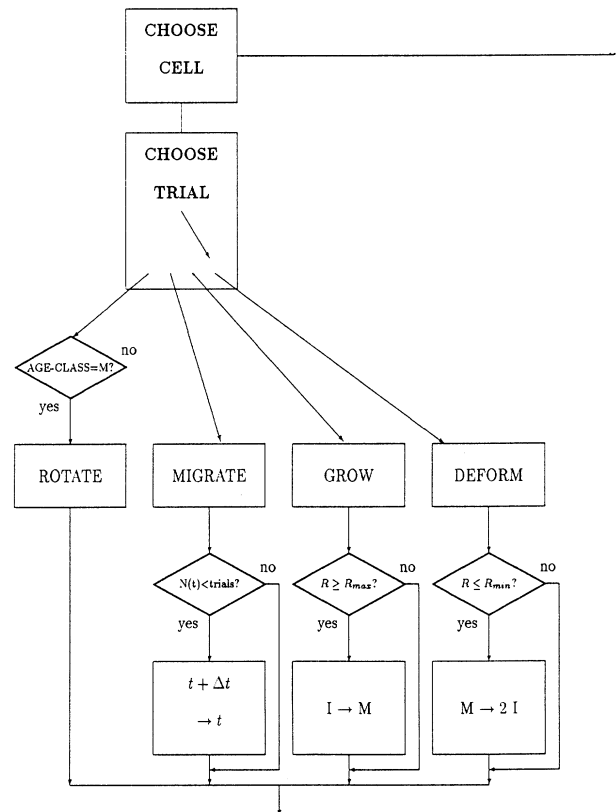


FIG. 34. Schematic flow chart of basic simulation algorithm.

rejection of every growth trial which leads to an overlap of the hard spheres.

DEFORM: This step changes both the distance  $d$  between the centers of the dumbbell shape and the radius  $R$  of each of the circles which make up the cell shape:

$$\begin{aligned}\hat{R}(n+1) &= R(n) - f^{IM}\eta \delta R, \\ d(n+1) &= d(n) + f^{IM}\eta \delta d(R(n), \delta R).\end{aligned}\quad (\text{A3})$$

$\delta d(R(n), \delta R)$  is determined from the equation area

$[d(n)] = \text{area}[d(n+1)]$ .  $\delta R$  is again drawn from the interval  $[0, \delta R_{\max}]$  and  $\eta$  is defined according to the Metropolis rule.

ROTATE:

$$\phi(n+1) = \phi(n) + \eta \delta \phi. \quad (\text{A4})$$

$\phi$  describes the orientation  $\hat{d}$  of an  $M$  cell. In three dimensions the Monte Carlo step has to be modified accordingly.

- 
- [1] M. Eigen, J. McCaskill, and P. Schuster, *J. Phys. Chem.* **92**, 6881 (1988).
- [2] M. Eigen, J. McCaskill, and P. Schuster, *Adv. Chem. Phys.* **75**, 142 (1989).
- [3] W. Jäger, H. Rost, and P. Tautu, *Biological Growth and Spread*, Lecture Notes in Biomathematics Vol. 38 (Springer, Heidelberg, 1980).
- [4] J. F. Crow, *Basic Concepts in Population, Quantitative, and Evolutionary Genetics* (W.H. Freeman and Company, New York, 1986).
- [5] R. Kree, B. Schaub, and B. Schmittmann, *Phys. Rev. A* **39**, 2214 (1989).
- [6] A. M. Turing, *Philos. Trans. R. Soc. London B* **237**, 37 (1952).
- [7] A. Gierer, *Socioeconomic Inequalities: Adaption and Application of a Theory of Biological Pattern Formation*, in *Pattern Formation by Dynamic Systems & Pattern Recognition*, edited by H. Haken (Springer, Heidelberg, 1979).
- [8] H. Meinhard, *Models of Biological Pattern Formations* (Academic, London, 1982).
- [9] S. A. Newman and H. L. Frisch, *Science* **205**, 108 (1979).
- [10] S. A. Newman, H. L. Frisch, and J. K. Percus, *J. Theor. Biol.* **134**, 183 (1988).
- [11] J. D. Murray, *Mathematical Biology* (Springer, Heidelberg, 1989).
- [12] M. Eden, in *Proceedings of the 4th Berkeley Symposium on Mathematics and Probability*, edited by J. Neyman (University of California Press, Berkeley, 1961), Vol. IV.
- [13] T. A. Witten and L. M. Sander, *Phys. Rev. Lett.* **47**, 1400 (1981).
- [14] W. Düchting and Th. Vogelsänger, *BioSystems* **18**, 79 (1985); W. Düchting, *Comput. Graphics* **14**, 505 (1990); W. Düchting, W. Ulmer, R. Lehrig, T. Ginsberg, and E. Dedeleit, *Strahlenther. Onkol.* **168**, 354 (1992).
- [15] P. Meakin, H. E. Stanley, and N. Ostrowski, *On Growth and Form—Fractal and Non-Fractal Patterns in Physics* (Martinus Nijhoff, Dordrecht, 1986).
- [16] M. Markus and B. Hess, *Nature* **347**, 111 (1990).
- [17] S. R. Hameroff, J. E. Dayhoff, F. Lahoz-Beltra, A. V. Samsonovich, and S. Rasmussen, *Computer* **10**, 30 (1992).
- [18] H. E. Schepers and M. Markus, *Physica A* **188**, 337 (1992).
- [19] A. Lindenmayer, *J. Theor. Biol.* **18**, 280 (1968).
- [20] G. T. Hermann and G. Rozenberg, *Developmental Systems and Languages* (North-Holland, New York, 1975).
- [21] G. M. Odell, G. Oster, P. Alberch, and B. Burnside, *Develop. Biol.* **85**, 446 (1981).
- [22] G. F. Oster, *J. Embryol. Exp. Morph.* **83**, Suppl., 329 (1984).
- [23] G. F. Oster and A. S. Perelson, *Sci. Suppl.* **8**, 35 (1987); G. F. Oster, *Cytoskeleton* **10**, 164 (1988).
- [24] M. S. Steinberg, *Symp. Soc. Study Dev. Growth* **22**, 321 (1964).
- [25] H. M. Phillips and M. S. Steinberg, *J. Cell. Sci.* **30**, 1 (1978).
- [26] R. J. Poole and M. S. Steinberg, *Dev. Biol.* **92**, 144 (1982).
- [27] M. S. Steinberg, *J. Exp. Zool.* **173**, 395 (1970).
- [28] M. S. Steinberg and T. J. Poole, in *Developmental Order: Its Origin and Regulation* (Alan R. Liss, Inc., New York, 1982), pp. 352–378.
- [29] N. S. Goel, and R. L. Thompson, *Computer Simulations of Self-Organization in Biological Systems* (Biddles Ltd., London, 1988).
- [30] F. Graner, *J. Theor. Biol.* **164**, 455 (1993).
- [31] F. Graner and Y. Sawada, *J. Theor. Biol.*, **164**, 477 (1993).
- [32] K. Binder, *Monte Carlo Methods in Statistical Physics* (Springer, Berlin, 1979).
- [33] M. P. Allen and D. J. Tildesley, *Computer Simulation of Liquids* (Clarendon Press, Oxford, 1987).
- [34] J. M. Hammersley and D. C. Handscomb, *Monte Carlo Methods* (Methuen & Co. Ltd., London, 1964).
- [35] L. L. Carter and E. D. Cashwell, *Particle Transport Simulation with the Monte Carlo Method*, ERDA Critical Review Series TID-26607 (U.S. Department of Energy, Washington, D.C., 1975).
- [36] T. E. Booth and E. D. Cashwell, *Nucl. Sci. Eng.* **71**, 128 (1979).
- [37] J. A. McCammon and S. Harvey, *Dynamics of Proteins and Nucleic Acids* (Cambridge University Press, Cambridge, 1987).
- [38] L. C. Junqueira and J. Carneiro, *Histologie* (Springer, Berlin, 1991).
- [39] P. F. Kruse and M. K. Patterson, *Tissue Culture* (Academic Press, New York, 1973).
- [40] J. M. Vasiliev and I. M. Gelfand, *Neoplastic and Normal Cells in Culture* (Cambridge University Press, Cambridge, 1981).
- [41] A. D. Bershadsky and J. M. Vasiliev, *Cytoskeleton* (Plenum Press, New York, 1988).
- [42] G. H. Sato, A. B. Pardee, and D. A. Sirbasku, *Growth of Cells in Hormonally Defined Media* (Cold Spring Harbor Laboratory, Cold Spring Harbor, 1982).
- [43] R. I. Freshney, *Culture of Animal Cells* (Alan R. Liss Inc., New York, 1983).

- [44] G. M. Edelman and J. P. Thiery, *The Cell in Contact: Adhesions and Junctions as Morphogenetic Determinants* (Wiley, New York, 1985).
- [45] G. M. Edelman, *Exp. Cell Res.* **161**, 1 (1985).
- [46] G. Edelman, *Annu. Rev. Cell Biol.* **2**, 81 (1986).
- [47] G. Edelman, *Topobiology* (Basic Books Inc., New York, 1988).
- [48] G. Edelman, *Spekt. d. Wissenschaft* **251**, 5 (1989).
- [49] N. Metropolis, A. W. Rosenbluth, M. N. Rosenbluth, A. H. Teller, and E. Teller, *J. Chem. Phys.* **21**, 1087 (1953).
- [50] L. J. Singer and G. L. Nicolson, *Science* **175**, 720 (1972).
- [51] G. Yagil (private communications).
- [52] K. Burridge, *Cancer Rev.* **4**, 18 (1986).
- [53] C. O'Neil, P. Jordan, and G. Ireland, *Cell* **44**, 489 (1986).
- [54] A. Ben-Ze'ev, J. L. R. Fernandez, G. Baum, and B. Gorodecki, in *Mechanisms of Differentiation*, edited by P. B. Fisher (CRC Press, New York, 1990).
- [55] B. Geiger, T. Volk, T. Volberg, and R. Bendori, *J. Cell Sci. Suppl.* **8**, 251 (1987).
- [56] D. Drasdo, Ph.D. thesis, University of Göttingen, 1993 (unpublished).
- [57] R. F. Brooks, in *Temporal Order*, edited by L. Rensing and N. I. Jaeger (Springer, Berlin, 1985).
- [58] B. Alberts, D. Bray, J. Lewis, M. Raff, K. Roberts, and J. D. Watson, *Molecular Biology of the Cell* (Garland, New York, 1989).
- [59] J. D. Watson, N. H. Hopkins, J. W. Roberts, J. A. Steitz, and A. M. Weiner, *Molecular Biology of the Gene*, 4th ed. (Benjamin Cummings, New York, 1987).
- [60] D. Drasdo and R. Kree (unpublished).
- [61] U. N. Riede, H. E. Schäfer, and H. Wehner, *Allgemeine und Spezielle Pathologie* (Thieme Verlag, New York, 1989).
- [62] M. Abercrombie and J. E. M. Heaysman, *Exp. Cell Res.* **6**, 292 (1954).
- [63] B. Westermark, *Int. J. Cancer* **12**, 438 (1974).
- [64] J. Folkman and A. Moscona, *Nature* **260**, 345 (1979).
- [65] R. O. Heynes, *Surfaces of Normal and Malignant Cells* (Wiley, New York, 1979).
- [66] S. A. Aaronson and G. J. Todaro, *Science*, **162**, 1024 (1968).
- [67] R. Kree (unpublished).
- [68] N. Brunet, D. Gourdjji, A. Tixier-Vidal, and A. Rizzino, *Role of Attachment and Spreading Factors: Effect of Fectuin on Proliferation and Prolactin Secretion by GH3 Cells and Primary Cultures of Normal Rat Pituitary Cells*, in Ref. [42].
- [69] J. M. Vasiliev, *Biochim. Biophys. Acta* **780**, 21 (1985).